

Impact of grids and dynamical cores in CESM2.2 on the surface mass balance of the Greenland Ice Sheet

Adam R. Herrington¹, Peter H. Lauritzen¹, Marcus Lofverstrom², William H. Lipscomb¹, Andrew Gettelman¹ and Mark A. Taylor³

¹National Center for Atmospheric Research, 1850 Table Mesa Drive, Boulder, Colorado, USA

²Department of Geosciences, University of Arizona, 1040 E. 4th Street, Tucson, Arizona USA

³Sandia National Laboratories, Albuquerque, New Mexico, USA

Key Points:

- The CESM2.2 release includes several enhancements to the spectral-element dynamical core, including two Arctic refined mesh configurations.
- Quasi-uniform unstructured** grids degrade the Greenland Ice Sheet mass balance compared to latitude-longitude grids, **at the conventional 1° resolution**.
- The refined Arctic meshes substantially improve the surface mass balance over **conventional grid resolutions**.

15 **Abstract**

16 Six different configurations, a mixture of grids and atmospheric dynamical cores
 17 available in the Community Earth System Model, version 2.2 (CESM2.2), are evaluated
 18 for their skill in representing the climate of the Arctic and the surface mass balance of
 19 the Greenland Ice Sheet (GrIS). The finite-volume dynamical core uses structured, latitude-
 20 longitude grids, whereas the spectral-element dynamical core is built on unstructured
 21 meshes, permitting grid flexibility such as quasi-uniform grid spacing globally. The 1°–
 22 2° latitude-longitude and quasi-uniform unstructured grids systematically overestimate
 23 both accumulation and ablation over the GrIS. Of these 1°–2° grids, the latitude-longitude
 24 grids outperform the quasi-uniform unstructured grids because they have more degrees
 25 of freedom to represent the GrIS. Two Arctic-refined meshes, with 1/4° and 1/8° refine-
 26 ment over Greenland, were developed for the spectral-element dynamical core and are
 27 documented here as newly supported configurations in CESM2.2. The Arctic meshes sub-
 28 stantly improve the simulated clouds and precipitation rates in the Arctic. Over Green-
 29 land, these meshes skillfully represent accumulation and ablation processes, leading to
 30 a more realistic GrIS surface mass balance. As CESM is in the process of transitioning
 31 away from conventional latitude-longitude grids, these new Arctic-refined meshes improve
 32 the representation of polar processes in CESM by recovering resolution lost in the tran-
 33 sition to quasi-uniform grids, albeit at increased computational cost.

34 **Plain Language Summary**

35 The mass balance of Earth's big ice sheets is crucially important for understand-
 36 ing controls on global sea-level rise. However, the scale of the processes needed to rep-
 37 resent ice sheet mass balance is challenging to resolve in conventional Earth System Mod-
 38 els. This study evaluates the ability of different grids and atmospheric solvers (i.e., the
 39 dynamical core) in CESM2.2 to resolve the surface mass balance (SMB) of the Green-
 40 land Ice Sheet. We show that the ongoing transition away from latitude-longitude grids,
 41 towards quasi-uniform unstructured grids in CESM2.2 leads to a degradation of the sim-
 42 ultated SMB. Two variable-resolution grids with enhanced resolution over Greenland are
 43 developed and incorporated into the release of CESM2.2, which substantially improves
 44 the SMB over the latitude longitude grids.

45 **1 Introduction**

46 General Circulation Models (GCMs) are powerful tools for understanding the me-
 47 teorology and climate of the high latitudes, which are among the most sensitive regions
 48 on Earth to global and environmental change. GCMs differ vastly in their numerical treat-
 49 ment of polar regions because of the so-called *pole problem* (Williamson, 2007). The pole
 50 problem refers to numerical instability arising from the convergence of meridian lines into
 51 polar singularities on latitude-longitude grids (e.g., Figure 1a, hereafter referred to as
 52 *lat-lon* grids). Depending on the numerics, methods exist to suppress this instability, and
 53 lat-lon grids may be advantageous for polar processes by representing structures with
 54 finer resolution than elsewhere in the computational domain. With the recent trend to-
 55 wards quasi-uniform unstructured grids, any potential benefits of lat-lon grids in polar
 56 regions may be lost (hereafter, *quasi-uniform* refers to approximately isotropic grids, in
 57 contrast to lat-lon grids, which are highly anisotropic due to the polar singularity). In
 58 this study, we evaluate a number of grids and dynamical cores (hereafter referred to as
 59 *dycores*) available in the Community Earth System Model, version 2.2 (CESM2.2; Dan-
 60 abasoglu et al., 2020), including new variable-resolution grids (i.e., grids with enhanced
 61 resolution over a particular region), to understand their impacts on the simulated Arctic
 62 climate. We focus specifically on the climate and surface mass balance of the Green-
 63 land Ice Sheet.

In the 1970s, the pole problem was largely defeated through the adoption of efficient spectral transform methods in GCMs (see Williamson, 2007, and references therein). These methods transform grid point fields into a global, isotropic representation in wave space, where linear operators (e.g., horizontal derivatives) in the (truncated) equation set can be solved exactly. While spectral transform methods are still used today, local numerical methods have become desirable for their ability to run efficiently on massively parallel systems. The pole problem has thus re-emerged in contemporary climate models that use lat-lon grids, and some combination of reduced grids (modified lat-lon grids, with cells near the polar singularity elongated in the zonal direction) and polar filters are necessary to ameliorate this numerical instability (Jablonowski & Williamson, 2011). Polar filters subdue the growth of unstable computational modes by applying additional damping to the numerical solution over polar regions. This damping reduces the effective resolution in polar regions such that the resolved scales are *approximately* the same everywhere on the grid. We emphasize *approximately*, since it is conceivable that marginal increases in effective resolution occur over polar regions in lat-lon grids, despite polar filtering, since resolved waves can be represented with more grid points than at lower latitudes.

Dycores built on lat-lon grids have some advantages over [dycores built on](#) unstructured grids. Lat-lon coordinate lines are orthogonal, and aligned with zonally symmetric circulations that characterize many large-scale features of Earth's atmosphere. Lauritzen et al. (2010) has experimented with rotating lat-lon models such that their coordinate lines no longer align with an idealized, zonally balanced circulation. For the finite-volume lat-lon dycore considered in this paper (hereafter *FV*), numerical errors were shown to be largest when the polar singularity is rotated into the baroclinic zone (45°N latitude), generating spurious wave growth much earlier in the simulation than for other rotation angles. This illustrates the advantages of coordinate surfaces aligned with latitude bands, albeit an extreme example where the polar singularity and the polar filter are also contributing to the spurious wave growth. The unstructured grids all generate spurious baroclinic waves earlier in the simulations than the (unrotated) lat-lon models, although the unstructured model considered in this paper, the spectral-element dycore (hereafter *SE*), holds a balanced zonal flow without spurious wave growth appreciably longer than the rotated FV experiments (Lauritzen et al., 2010). And unlike FV, the SE dycore has the same error characteristics regardless of how the grid is rotated.

The polar filter in the FV model impedes efficiency at large processor (CPU) counts because it requires a spectral transform, which [has a](#) large communication overhead (Suarez & Takacs, 1995; Dennis et al., 2012). Unstructured grids support quasi-uniform grid spacing globally, and there is no pole problem (e.g., Figure 1c). [This is in part why](#) unstructured grids are becoming more common; their improved performance on massively parallel systems and lack of constraints on grid structure (Taylor et al., 1997; Putman & Lin, 2007; Wan et al., 2013). This increased grid flexibility allows for the adoption of variable-resolution grids (e.g., Figure 2; hereafter abbreviated as *VR*), sometimes referred to as regional grid refinement. In principle, grid refinement over polar regions can make up for any loss of resolution in transitioning away from lat-lon grids (e.g., Figure 2). However, local grid refinement comes at the cost of a smaller CFL-limited time step in the refined region; the CFL-condition — short for Courant–Friedrichs–Lowy condition — is a necessary condition for numerical stability when using discrete data in time and space.

We emphasize that the pole problem is a distinctive feature of the dycore in atmospheric models. Polar filters do not directly interfere with the physical parameterizations, nor do they have any bearing on the surface models; e.g., the land model can take full advantage of the greater number of grid cells in polar regions on lat-lon grids. This is particularly relevant for the surface mass balance ([SMB; the integrated sum of precipitation and runoff](#)) of the Greenland Ice Sheet, which relies on hydrological processes represented in the land model.

The SMB of the Greenland Ice Sheet (hereafter *GrIS*) is determined by processes occurring over a range of scales that are difficult to represent in GCMs (Pollard, 2010). GrIS precipitation is concentrated at the ice-sheet margins, where steep topographic slopes drive orographic precipitation. The truncated topography used by low resolution GCMs enables moisture to penetrate well into the GrIS interior, manifesting as a positive precipitation bias [in the interior](#) (Pollard & Groups, 2000; Van Kampenhout et al., 2019). GrIS ablation areas ([marginal regions where the annual SMB is negative](#)) are typically less than 100 km wide and are confined to low-lying areas or regions with low precipitation. These narrow ablation zones are not fully resolved in low-resolution GCMs, and may further degrade the simulated SMB. [More recently, GCMs such as CESM and the NASA Goddard Institute for Space Studies GCM \(Alexander et al., 2019\), have implemented an elevation class downscaling scheme for computing the SMB. The downscaling helps to resolve to these narrow ablation zones in GCMs \(Sellevold et al., 2019\), but large SMB biases remain.](#) For example, CESM, version 2.0 (CESM2) underestimates ablation in the northern GrIS, leading to unrealistic ice advance when run with an interactive ice sheet component (Lofverstrom et al., 2020).

Regional climate models (RCMs) are commonly relied upon to provide more accurate SMB estimates. The limited area domain used by RCMs permits the use of high-resolution grids capable of resolving SMB processes, and can skillfully simulate the GrIS SMB (Box et al., 2004; Rae et al., 2012; Van Angelen et al., 2012; Fettweis et al., 2013; Mottram et al., 2017; Noël et al., 2018). However, unlike GCMs, RCMs are not a freely evolving system, and the atmospheric state must be prescribed at the lateral boundaries of the model domain. The inability of the RCM solution to influence larger-scale dynamics outside the RCM domain (due to the prescribed boundary conditions) severely limits this approach from properly representing the role of the GrIS in the climate system. In addition, the boundary conditions are derived from a separate host model, which introduces inconsistencies due to differences in model design between the host model and the RCM.

In order to retain the benefits of RCMs in a GCM, Van Kampenhout et al. (2019) used the VR capabilities of the SE dycore in CESM, generating [grids](#) where Greenland is represented with [up to](#) $1/4^\circ$ resolution, and elsewhere with the more conventional 1° resolution. The simulated SMB compared favorably to the SMB from RCMs and observations. The VR approach is therefore emerging as a powerful tool for simulating and understanding the GrIS and its response to different forcing scenarios.

The SE dycore has been included in the model since CESM version 1, but has been under active development ever since. This includes the switch to a dry-mass vertical coordinate (Lauritzen et al., 2018) and incorporation of an accelerated multi-tracer transport scheme (Lauritzen et al., 2017), made available in CESM2. This paper documents several additional enhancements to the SE dycore as part of the release of CESM2.2. These include three new VR configurations (Figure 2), two Arctic meshes and a Contiguous United-States mesh (**CONUS**; featured in Pfister et al. (2020)). While there are dozens of published studies using VR in CESM (e.g., Zarzycki et al., 2014; Rhoades et al., 2016; Gettelman et al., 2017; Burakowski et al., 2019; Bambach et al., 2021), these studies either used development code or collaborated closely with model developers. CESM2.2 is the first code release that contains out-of-the-box VR functionality.

This study compares the representation of Arctic regions using the SE and FV dycores in CESM2.2 (see description below), as these two dycores treat high latitudes (i.e., the pole problem) in different ways. Section 2 documents the grids, dycores, and physical parameterizations used in this study, and also describes the experiments, datasets, and evaluation methods. Section 3 analyzes the results of the experiments, and Section 4 provides a general discussion and conclusions.

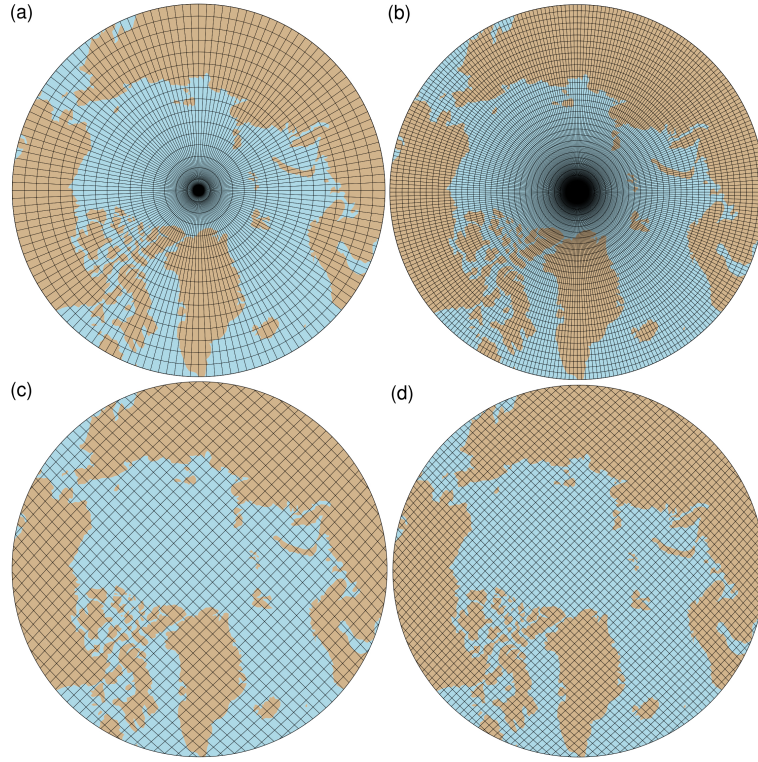


Figure 1. Computational grids for the 1° – 2° lat-lon and quasi-uniform unstructured grids in this study. Grids names after Table 1, (a) 2° lat-lon grid (f19), (b) 1° lat-lon grid (f09), (c) 1° quasi-uniform unstructured grid with reduced physics resolution (ne30pg2) and (d) 1° quasi-uniform unstructured grid (ne30pg3).

168 2 Methods

169 CESM2.2 is a CMIP6-class (Coupled Model Intercomparison Project Phase 6; Eyring
 170 et al., 2016) Earth System Model maintained by the National Center for Atmosphere Re-
 171 search. CESM2.2 contains sub-component models for the atmosphere, land, ocean, sea-
 172 ice, and land-ice, and can be configured to run with varying degrees of complexity. All
 173 simulations described in this study use an identical transient 1979-1998 Atmospheric Model
 174 Inter-comparison Project (AMIP) configuration, with prescribed monthly sea-surface tem-
 175 perature and sea ice following Hurrell et al. (2008). In CESM terminology, AMIP sim-
 176 ulations use the FHIST computational set and run out of the box in CESM2.2. The land-
 177 ice component is not dynamically active in FHIST. However, the surface mass balance
 178 is computed by the land model before being passed to the land-ice component; FHIST
 179 includes the functionality to simulate the surface mass balance of the Greenland Ice Sheet.

180 2.1 Dynamical cores

181 The atmospheric component of CESM2.2 (Danabasoglu et al., 2020), the Commu-
 182 nity Atmosphere Model, version 6.3 (CAM6; Gettelman et al., 2019; Craig et al., 2021),
 183 supports several different atmospheric dynamical cores. These include dycores on lat-
 184 lon grids, such as finite-volume (FV; Lin, 2004) and Eulerian spectral transform (EUL;
 185 Collins et al., 2006) models, and dycores built on unstructured grids, including spectral-
 186 element (SE; Lauritzen et al., 2018) and finite-volume 3 (FV3; Putman & Lin, 2007) mod-
 187 els. This study compares the performance of the SE and FV dycores, omitting the EUL

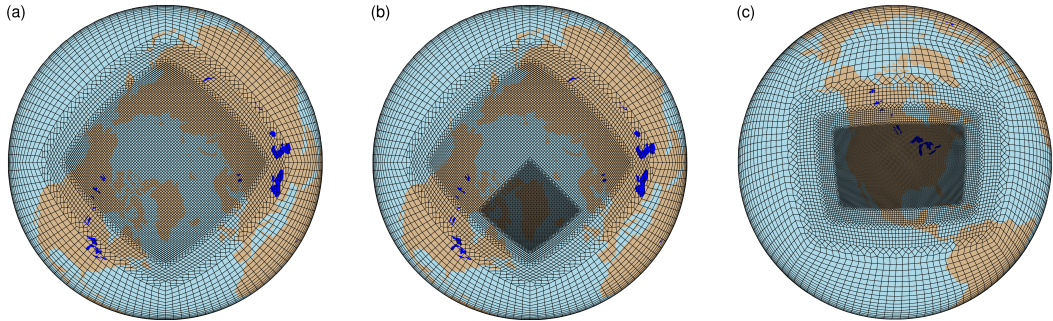


Figure 2. Variable-resolution grids available in CESM2.2, (a) **Arctic**, (b) **Arctic - GrIS** and (c) **CONUS**. Note what is shown is the element grid; the computational grid has 3×3 independent grid points per element.

and FV3 dycores. CESM2 runs submitted to CMIP6 used the FV dycore, whereas the SE dycore is often used for global high-resolution simulations (e.g., Small et al., 2014; Bacmeister et al., 2016; Chang et al., 2020) due to its higher throughput on massively parallel systems (Dennis et al., 2012).

2.1.1 Finite-volume (FV) dynamical core

The FV dycore integrates the [hydrostatic](#) equations of motion using a finite-volume discretization on a spherical lat-lon grid (Lin & Rood, 1997). The 2D dynamics evolve in floating Lagrangian layers that are periodically mapped to an Eulerian reference grid in the vertical (Lin, 2004). Hyperviscous damping is applied to the divergent modes, and is increased in the top few layers (referred to as a *sponge layer*) to prevent undesirable interactions with the model top, such as wave reflection (Lauritzen et al., 2011). A polar filter damps computational instability due to the convergence of meridians, permitting a longer time step. It takes the form of a Fourier filter in the zonal direction, with the damping coefficients increasing monotonically in the meridional direction (Suarez & Takacs, 1995). The form of the filter is designed to slow down the propagation of large zonal wave-numbers to satisfy the CFL condition of the shortest resolved wave at some reference latitude.

2.1.2 Spectral-element (SE) dynamical core

The SE dycore integrates the [hydrostatic](#) equations of motion using a high-order continuous Galerkin method (Taylor et al., 1997; Taylor & Fournier, 2010). The computational domain is a cubed-sphere grid ([A cubed-sphere grid is obtained by projecting each face of a cube onto a sphere](#)) tiled with quadrilateral elements (see Figure 2). Each element contains a fourth-order basis set in each horizontal direction, with the solution defined at the roots of the basis functions, the Gauss-Lobatto-Legendre quadrature points. This results in 16 nodal points per element, with 12 of the points lying on the (shared) element boundary. Communication between elements uses the direct stiffness summation (Canuto et al., 2007), which applies a numerical flux to the element boundaries to reconcile overlapping nodal values and produce a continuous global basis set.

As with the FV dycore, the dynamics evolve in floating Lagrangian layers that are subsequently mapped to an Eulerian reference grid. A dry mass vertical coordinate was recently implemented for thermodynamic consistency with condensates (Lauritzen et al., 2018). The 2D dynamics have no implicit dissipation, and so hyperviscosity operators

220 are applied to all prognostic variables to remove spurious numerical errors (Dennis et
221 al., 2012). Laplacian damping is applied in the sponge layer.

222 SE is a next generation of dycore, and is less mature than the FV dycore due to
223 its shorter history. In CESM2.2, the SE numerics have been enhanced relative to CESM2.0
224 to mitigate spurious noise over topography. These algorithmic changes are described in
225 Appendix A. Future versions of CESM will likely continue to include further optimiza-
226 tions and enhancements to the (nascent) SE dycore.

227 The SE dycore supports regional grid refinement via its VR configuration, requir-
228 ing two enhancements over quasi-uniform resolution grids. First, as the numerical vis-
229 cosity increases with resolution, explicit hyperviscosity relaxes according to the local el-
230 ement size, reducing in strength by an order of magnitude per halving of the grid spac-
231 ing. A tensor-hyperviscosity formulation is used (Guba et al., 2014), which adjusts the
232 coefficients in two orthogonal directions to more accurately target highly distorted quadri-
233 lateral elements. Second, the topography boundary conditions are smoothed in a way
234 that does not excite grid scale modes, and so the NCAR topography software (Lauritzen
235 et al., 2015) has been modified to scale the smoothing radius by the local element size,
236 resulting in rougher topography in the refinement zone.

237 When using the SE dycore with quasi-uniform grid spacing, the SE tracer trans-
238 port scheme is replaced with the Conservative Semi-Lagrangian Multi-tracer transport
239 scheme (CSLAM) (Lauritzen et al., 2017). Atmospheric tracers have large, nearly dis-
240 continuous horizontal gradients that are difficult to represent with spectral methods, which
241 are prone to oscillatory “Gibbs-ringing” errors (Rasch & Williamson, 1990). CSLAM has
242 improved tracer property preservation and accelerated multi-tracer transport. It uses a
243 separate grid from the spectral-element dynamics, dividing each element into 3×3 con-
244 trol volumes with quasi-equal area. The physical parameterizations are computed from
245 the state on the CSLAM grid, which has clear advantages over the original SE dycore
246 in which the physics are evaluated at Gauss-Lobatto-Legendre points (Herrington et al.,
247 2018). CSLAM advection is not an available option in the VR configuration, which in-
248 stead uses the standard SE tracer transport scheme with the physics evaluated at Gauss-
249 Lobatto-Legendre points.

250 2.2 Physical parameterizations

251 All simulations in this study use the CAM6 physical parameterization package (hereafter
252 referred to as the *physics*; Gettelman et al., 2019). The physics in CAM6 differs from
253 its predecessors through the incorporation of high-order turbulence closure, Cloud Lay-
254 ers Unified by Binormals (CLUBB; Golaz et al., 2002; Bogenschutz et al., 2013), which
255 jointly acts as a planetary boundary layer, shallow convection, and cloud macrophysics
256 scheme. CLUBB is coupled with the MG2 microphysics scheme (Gettelman & Morri-
257 son, 2015; Gettelman et al., 2015), which computes prognostic precipitation and uses clas-
258 sical nucleation theory to represent cloud ice for improved cloud-aerosol interactions. Deep
259 convection is parameterized using a convective quasi-equilibrium mass flux scheme (Zhang
260 & McFarlane, 1995; Neale et al., 2008) and includes convective momentum transport (Richter
261 et al., 2010). Boundary layer form drag is modeled after Beljaars et al. (2004), and orog-
262 graphic gravity wave drag is represented with an anisotropic method informed by the
263 orientation of topographic ridges at the sub-grid scale (the ridge orientation is derived
264 from a high-resolution, global topography dataset (J. J. Danielson & Gesch, 2011)).

265 Initial simulations with the SE dycore produced weaker shortwave cloud forcing
266 relative to the tuned finite-volume dycore in the standard CESM2 configuration. The
267 SE dycore in CESM2.2 therefore has two CLUBB parameter changes to provide more
268 realistic cloud forcing and top-of-atmosphere radiation balance. We reduced the width
269 of the sub-grid distribution of vertical velocity (`clubb_gamma` = 0.308 → 0.270) and
270 also reduced the strength of the damping for horizontal component of turbulent energy

grid name	dycore	Δx_{eq} (km)	Δx_{fine} (km)	Δt_{phys} (s)	cost(25 nodes)	cost(50 nodes)
f19	FV	278	-	1800	436.66	-
f09	FV	139	-	1800	1534.57	2024.24
ne30pg2	SE-CSLAM	167	-	1800	1497.26	1683.97
ne30pg3	SE-CSLAM	111	-	1800	1890.48	2090.43
ne30pg3*	SE-CSLAM	111	-	450	-	-
Arctic	SE	111	28	450	15947.41	16675.45
Arctic – GrIS	SE	111	14	225	40305.03	41036.67

Table 1. Grids and dycores used in this study. Δx_{eq} is the average equatorial grid spacing, Δx_{fine} is the grid spacing in the refined region (if applicable), and Δt_{phys} is the physics time step. FV refers to the finite-volume dycore, SE the spectral-element dycore, and SE-CSLAM the spectral-element dycore with CSLAM tracer advection. The FV dycore uses lat-lon grids, whereas the SE and SE-CSLAM dycores run on unstructured grids. We use the ne30pg3 grid for two runs with different values of Δt_{phys} . The last columns provide the computational costs in core hours per simulated year (CHPSY). The costs are from single month runs using 25 nodes and 50 nodes on the Cheyenne supercomputer (Computational and Information Systems Laboratory, 2017).

(`clubb_c14` = 2.2 → 1.6) to increase cloudiness. For a description of how CLUBB parameters impact the simulated climate, see Guo et al. (2015).

2.3 Grids

We evaluate model simulations on six different grids in this study (Table 1). The FV dycore is run with nominal 1° and 2° grid spacing, referred to as f09 and f19, respectively (Figure 1a,b). We also run the 1° equivalent of the SE-CSLAM grid, referred to as ne30pg3 (Figure 1d), where *ne* refers to a grid with *ne* × *ne* quadrilateral elements per cubed-sphere face, and *pg* denotes that there are *pg* × *pg* control volumes per element for computing the physics. We run an additional 1° SE-CSLAM simulation with the physical parameterizations computed on a grid with 2 × 2 control volumes per element, ne30pg2 (Figure 1c; Herrington et al., 2019, note CSLAM is still run on the 3 × 3 control volume grid).

Three VR meshes were developed for the CESM2.2 release to support grid refinement over the Arctic and the United States (Figure 2). This paper serves as the official documentation of these grids. The VR meshes were developed using the software package SQuadgen (<https://github.com/ClimateGlobalChange/squadgen>). The Arctic grid is a 1° grid with 1/4° regional refinement over the broader Arctic region (when using degrees to describe the resolution of unstructured grids, degrees refers to degrees at the equator). The Arctic–GrIS grid is identical to the Arctic grid, but with an additional patch covering the island of Greenland with 1/8° resolution. The CONUS grid contains 1/8° refinement over the United States, and 1° everywhere else. The CONUS grid is not discussed any further in this paper; see Pfister et al. (2020) for simulations with the CONUS grid.

The accuracy of the simulated surface mass balance is expected to be sensitive to grid resolution. Figure 3a shows the average grid spacing over the Greenland Ice Sheet (*GrIS* hereafter), in all six grids, as well as two grids pertaining to the Regional Atmospheric Climate Model (RACMO; Noël et al., 2018, 2019), which are used for validation purposes in this study (Table 2). The ne30pg2 grid has the coarsest representation with an average grid spacing (Δx) of $\Delta x = 160$ km, and the Arctic – GrIS grid has the highest resolution with an average grid spacing of $\Delta x = 14.6$ km, similar to the 11 km grid spacing of the RACMO2.3 grid. The ne30pg3 grid has an average $\Delta x = 111.2$ km,

302 substantially coarser than the **f09** grid, with an average $\Delta x = 60$ km. Although **ne30pg3**
 303 and **f09** have similar average grid spacing over the entire globe, and comparable com-
 304 putational costs, the convergence of meridians on the FV grid enhances the resolution
 305 over the GrIS. The **Arctic** grid has an average grid spacing of $\Delta x = 27.8$ km.

306 The physics time step depends on the grid resolution. Increased horizontal reso-
 307 lution permits faster vertical velocities that reduce characteristic time scales, so the physics
 308 time step is reduced to avoid large time truncation errors (Herrington & Reed, 2018).
 309 The **Arctic** and **Arctic – GrIS** grids are run with a $4\times$ and $8\times$ reduction in physics
 310 time step relative to the default 1800 s time step used in the 1° and 2° grids (Table 1).

311 All grids and dycores in this study use 32 hybrid pressure-sigma levels in the ver-
 312 tical, with a model top of 2 hPa or about 40 km. However, any grid or dycore can in prin-
 313 ciple be run with a higher model top or finer vertical resolution.

314 2.4 Computational costs

315 The last columns of Table 1 provides cost estimates for the different grids and dy-
 316 cores. The costs, expressed as core hours per simulated year (CHPSY), are taken from
 317 single month runs of FHIST, with no i/o, and using 25 nodes (900 tasks) and 50 nodes
 318 (1800 tasks) on the Cheyenne supercomputer (Computational and Information Systems
 319 Laboratory, 2017). 25 nodes is on the low side for a typical multi-decadal climate sim-
 320 ulation at 1° resolution, but it's the largest number of tasks that can be supported by
 321 the **f19** grid, and we chose to fix the number of tasks across all grids for the purposes
 322 of comparing their costs. We also provide costs using 50 nodes, excluding **f19**, to pro-
 323 vide a more practical cost estimate for longer climate integrations. There are probably
 324 better approaches for comparing costs across different grids and dycores, e.g., holding
 325 fixed the number of grid columns per task, but it is beyond the scope of this study.

326 The cheapest grid is the **f19** grid at 436.66 CHPSY, as this is the only grid run-
 327 ning with 2° dynamics. The **f09** grid costs 1534.57 CHPSY using 25 nodes, which is no-
 328 ticeably cheaper than **ne30pg3** at 1890.48 CHPSY. The **ne30pg2** grid is 20% cheaper than
 329 the **ne30pg3** grid, in both the 25 node and 50 node runs, consistent with previous es-
 330 timates (Herrington & Reed, 2018). The FV model is known to be cheaper than SE at
 331 small core counts, whereas SE is more efficient than FV at large core counts due to its
 332 improved scalability (Dennis et al., 2005, 2012). In the more conventional 50 node runs,
 333 **f09** costs are much more similar to **ne30pg3**, due to a 30% cost increase in **f09** relative
 334 to the 25 node run (Table 1). The **Arctic** grid is an order of magnitude more expen-
 335 sive than the lat-lon and quasi-uniform grids, at about 16k CHPSY, whereas the **Arctic–**
 336 **GrIS** grid is a more than twice that (40k CHPSY). Note that all timing numbers are from
 337 runs without threading. The **f09** grid is the only grid that runs out-of-the-box with thread-
 338 ing; holding the number of tasks fixed leads to a 4%–6.5% reduction in CHPSY com-
 339 pared to runs without threading.

340 2.5 Simulated surface mass balance (SMB)

341 CESM simulates the GrIS SMB as the sum of ice accumulation and ice ablation.
 342 The latter contains contributions from sublimation and liquid runoff from ice melt. Liq-
 343 uid precipitation and liquid runoff may also contribute to ice accumulation by penetrat-
 344 ing pore spaces in the snowpack/firn layer and freeze, forming ice lenses. These relevant
 345 SMB processes are represented by different CESM components, but it is the Commu-
 346 nity Land Model, version 5 (CLM; Lawrence et al., 2019), that aggregates these processes
 347 and computes the SMB.

348 CLM runs on the same grid as the atmosphere, and uses a downscaling technique
 349 to account for sub-grid variability in SMB. In short, the ice sheet patch in a CLM grid
 350 cell is subdivided into 10 elevation classes (ECs), each with a distinct surface energy bal-

351 ance and SMB. The area fraction of each EC is computed from the CISM initial con-
 352 ditions, which are based on a high-resolution dataset of the observed, modern extent and
 353 thickness of the GrIS (Morlighem et al., 2014). Note that for configurations with a dy-
 354 namically active ice sheet, the area fractions are continuously updated throughout the
 355 run to reflect the evolving ice sheet geometry in CISM. The near-surface air tempera-
 356 ture, humidity, and air density are calculated for each EC using an assumed lapse rate
 357 and the elevation difference from the grid-cell mean. Precipitation from CAM is repar-
 358 titioned into solid or liquid based on the surface temperature of the EC; precipitation
 359 falls as snow for temperatures between $T < -2^{\circ}$ C, as rain for $T > 0^{\circ}$ C, and as a lin-
 360 ear combination of rain and snow for temperatures between -2° C and 0° C.

361 Changes in ice depth, not snow depth, count toward the SMB. Snow accumulation
 362 in each EC is limited to a depth of 10 m liquid water equivalent. Any snow above the
 363 10 m cap contributes towards ice accumulation, and refreezing of liquid water within the
 364 snowpack is an additional source of ice. Surface ice melting (after melting of the over-
 365 lying snow) yields a negative SMB. Integrating over all ECs, weighting by the area frac-
 366 tions, provides a more accurate SMB than would be found using the grid-cell mean el-
 367 evation. For a more detailed description of how the SMB is computed in CESM, we re-
 368 fer the reader to Lipscomb et al. (2013); Sellevold et al. (2019); van Kampenhout et al.
 369 (2020); Muntjewerf et al. (2021).

370 Since snow in the accumulation zone must reach the cap to simulate a positive SMB,
 371 the snow depths on the VR grids were spun up by forcing CLM in standalone mode, cy-
 372 cling over data from a 20-year Arctic FHIST simulation ([with perpetual 1979 bound-](#)
 373 [ary conditions](#)) for about 500 years. The 1° – 2° lat-lon and quasi-uniform unstructured
 374 grids are initialized with the SMB from an existing f09 spun-up initial condition.

375 2.6 Validation Datasets

376 We use several [validation](#) datasets (Table 2) to assess the performance of the sim-
 377 ulations. The ERA5 reanalysis product (Copernicus, 2019) is used for validating the large-
 378 scale circulation and extreme precipitation events. Clouds and radiation fields are val-
 379 idated using remote sensing products, the CERES-EBAF ED4.1 (Loeb et al., 2018) and
 380 the CALIPSO-GOCCP (Chepfer et al., 2010) datasets, respectively.

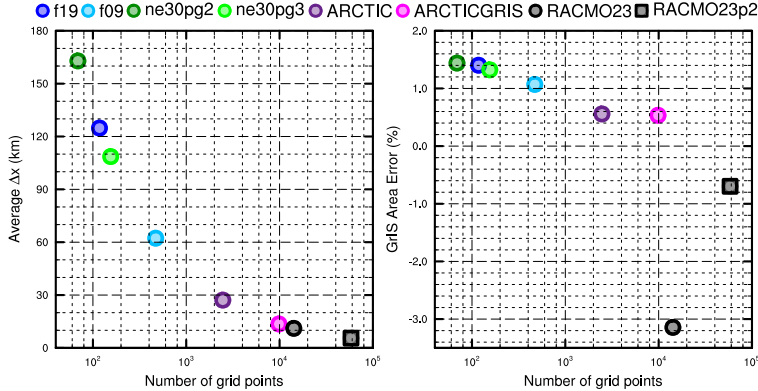
381 SMB datasets are gathered from multiple sources. RACMO, version 2.3 11km (RACMO23;
 382 Noël et al., 2015) and version 2.3p2 5.5km (RACMO2.3p2; Noël et al., 2018, 2019) are
 383 RCM simulations targeting Greenland, forced by ERA renalyses products at the domain's
 384 lateral boundaries. The RACMO simulations have been shown to perform skillfully against
 385 observations and are often used as modeling targets (e.g., Evans et al., 2019; van Kam-
 386 penhout et al., 2020). The RACMO datasets are used along with the CERES-EBAF prod-
 387 uct to validate the radiative fluxes around Greenland.

388 In-situ SMB (snow pit and ice cores) and [remote sensing datasets](#) (e.g., IceBridge
 389 radar accumulation dataset) are maintained in The Land Ice Verification and Validation
 390 toolkit (LIVVkit), version 2.1 (Evans et al., 2019). However, these point-wise measure-
 391 ments are difficult to compare to model output spanning several different grids, especially
 392 since the SMB from each elevation class is not available from the model output. We used
 393 a nearest-neighbor technique for an initial analysis, which showed that the model biases
 394 are similar to those computed using the RACMO datasets. Because of the uncertainty
 395 of comparing gridded fields to point-wise measurements, and the lack of information added
 396 with regard to model biases, we omitted these datasets from our analysis.

397 2.7 SMB Analysis

398 We seek to integrate SMB components over a GrIS ice mask and to diagnose their
 399 contributions to the GrIS mass budget. However, the ice masks vary across the grids,

data product	years used in this study	resolution	citation
ERA5	1979-1998	1/4°	Copernicus (2019)
CERES-EBAF ED4.1	2003-2020	1°	Loeb et al. (2018)
CALIPSO-GOCCP	2006-2017	2°	Chepfer et al. (2010)
RACMO2.3	1979-1998	11 km	Noël et al. (2015)
RACMO2.3p2	1979-1998	5.5 km	Noël et al. (2019)

Table 2. Description of validation datasets used in this study.**Figure 3.** The spatial properties of the GrIS as represented by different grids in this study. (Left) approximate average grid spacing over GrIS, (right) GrIS area error, computed as the relative differences from the reference dataset described in the text. Also included are the two RACMO grids used for validation (see Table 2).

especially in comparison to the RACMO3.2 ice mask, whose total area is about 3% less than that of the reference dataset (i.e., the GrIS initial conditions in CISM; Figure 3b). CLM's dataset creation tool generates the model ice mask by mapping the reference dataset to the target grid using the Earth System Modeling Framework (ESMF) first-order conservative remapping algorithm (Team et al., 2021). The figure suggests that the mapping errors are less than 1.5% across the CESM2.2 grids. The area errors in Figure 3b may seem small, but even 1–2% area differences can lead to large differences in integrated SMB (Hansen et al., 2022).

We have taken a common-ice-mask approach by mapping all model fields to the lowest-resolution grids, i.e., the `f19` and `ne30pg2` grids, and integrating over these low-resolution ice masks. The use of low-resolution common ice masks is a conservative decision, and is justified because we seek to use first-order remapping algorithms to map fields to the common ice mask, which is not generally reliable when mapping to a higher-resolution grid than the source grid. We use two remapping algorithms: ESMF first-order conservative and the TempestRemap (Ullrich & Taylor, 2015) high-order monotone algorithm. Since mapping errors are sensitive to grid type, we evaluate all quantities on both common ice masks, the `f19` and `ne30pg2` masks. Thus, we evaluate an integrated quantity on a given grid up to four times to estimate the uncertainty due to differences in grid type and remapping algorithms.

The SMB is expressed in a form that is agnostic of water phase, a total water mass balance, to facilitate comparisons across different grids with different ice masks and to increase consistency with the variables available in the RACMO datasets. The SMB for total water can be expressed as:

$$\text{SMB} = \text{accumulation} + \text{runoff} + \text{evaporation} + \text{sublimation}, \quad (1)$$

423 where all terms have consistent sign conventions (positive values contribute mass, and
 424 negative values reduce mass). The accumulation source term refers to the combined solid
 425 and liquid precipitation, runoff refers to the liquid water sink, and evaporation/sublimation
 426 is the vapor sink. Since the runoff term aggregates many processes, we isolate the melt-
 427 ing contribution by also tracking the combined melt of snow and ice.

428 The total water SMB (equation 1) is different from the SMB internally computed
 429 by CLM and described in section 2.5, which only tracks ice mass. We do not use CLM's
 430 internally computed SMB in this study. Rather, we utilize the components of the inter-
 431 nally computed SMB to construct the total water SMB.

432 We consider two approaches for mapping and integrating the SMB components over
 433 the common ice masks:

- 434 1. Map the grid-cell mean quantities to the common grid, and integrate the mapped
 435 fields over the common ice masks.
- 436 2. Map the patch-level quantities (i.e., the state over the ice fractional component
 437 of the grid cell) to the common grid, and integrate the mapped fields over the com-
 438 mon ice masks.

439 Note that we are mapping to low-resolution grids that have larger GrIS areas than
 440 the source grids (Figure 3b). Since the components of equation 1 are not confined to the
 441 ice mask, method 1 reconstructs the SMB over the portion of the common ice mask that
 442 is outside the ice mask on the source grid. While this may be a an acceptable way to re-
 443 construct the mass source terms over different ice masks, ice melt is zero outside the source
 444 ice mask, and so method 1 will underestimate the mass sink term. This underestima-
 445 tion is systematic in method 2, where all variables are exclusive to the ice mask; map-
 446 ping to a lower-resolution grid will dilute a field of non-zero values over the ice mask with
 447 a field of zeros outside the ice mask. However, patch-level values for processes exclusive
 448 to the ice mask (e.g., ice melt) will on average have larger magnitudes than the grid-mean
 449 quantities used in method 1.

450 The different error characteristics of the two methods are used to further diversify
 451 the ensemble. Each of the four regridding combinations (with conservative and high-order
 452 remapping to the f09 and ne30pg2 grids) are repeated with each method, resulting in
 453 (up to) eight values for each integrated quantity. Unfortunately, the patch-level values
 454 of evaporation/sublimation are not available from the model output, and we estimate
 455 their contribution by zeroing out the field for grid cells that have no ice, prior to map-
 456 ping to the common ice mask. This will degrade the SMB estimates using method 2, but
 457 we are more interested in characterizing the behavior of individual processes across grids
 458 and dycores, expressed as the components of the SMB, rather than the SMB itself.

459 3 Results

460 3.1 Tropospheric temperatures

461 Before delving into the simulated Arctic climate conditions, we assess the global
 462 mean differences between the various grids and dycores. Figure 4 shows 1979–1998 an-
 463 nual mean, zonal mean height plots of temperature, expressed as differences between 1°–
 464 2° lat-lon and quasi-uniform unstructured grids and dycores. The f09 grid is warmer
 465 than the f19 grid, primarily in the mid-to-high latitudes throughout the depth of the
 466 troposphere. This is a common response to increasing horizontal resolution in GCMs (Pope
 467 & Stratton, 2002; Roeckner et al., 2006). Herrington and Reed (2020) have shown that
 468 this occurs in CAM due to higher resolved vertical velocities which, in turn, generate more
 469 condensational heating in the CLUBB macrophysics. The right panel in Figure 4a sup-

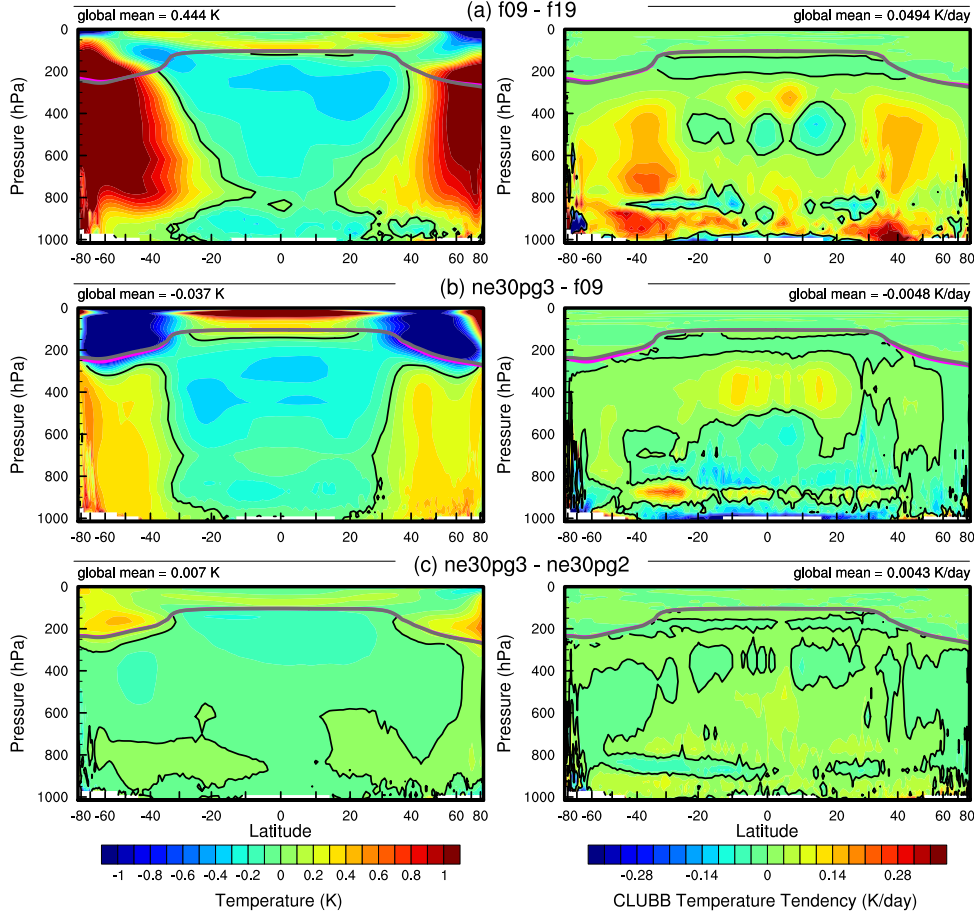


Figure 4. 1979–1998 annual mean temperature (left column) and CLUBB temperature tendencies (right column) in zonal mean height space, expressed as differences between the various $1^{\circ} - 2^{\circ}$ grids. The thick grey and magenta lines are the tropopause for the control run and the test run, respectively.

ports this interpretation, showing an increase in the climatological CLUBB heating at all latitudes in the **f09** grid, but with the largest increase in the mid-latitudes.

As the SE dycore is less diffusive than the FV dycore, the resolved vertical velocities are larger in the SE dycore, and so the **ne30pg3** troposphere is modestly warmer than **f09** (Figure 4b). The stratosphere responds differently, with **ne30pg3** much cooler than **f09** in the mid-to-high latitudes. Figure 4c also shows small temperature differences between **ne30pg3** and **ne30pg2**, with **ne30pg3** slightly warmer near the tropopause at high latitudes. This is consistent with the similar climates found for these two grids by Herrington et al. (2019).

Comparing the VR grids to the [lat-lon and quasi-uniform](#) grids is complicated because we simultaneously increase the resolution and reduce the physics time-step, both of which influence the solution (Williamson, 2008). We therefore run an additional **ne30pg3** simulation with the shorter physics time step used in the **Arctic** grid (450 s), referred to as **ne30pg3*** (Table 1). Figure 5a shows the difference between **ne30pg3*** and **ne30pg3** for climatological summer temperatures in zonal-mean height space. The troposphere is warmer with the reduced time step, and the mechanism is similar in that the shorter

486 time step increases resolved vertical velocities (not shown) and CLUBB heating (right
 487 panel in Figure 5a). Figure 5b shows the difference in climatological summer temper-
 488 ature between the **Arctic** grid and the **ne30pg3*** grid. With the same physics time step,
 489 the greater condensational heating and warmer temperatures are confined to the refined
 490 Arctic region.

491 We note that there is not perfect alignment of the CLUBB heating anomalies and
 492 the temperature anomalies in Figures 4 & 5. This leaves some uncertainty as to whether
 493 CLUBB is solely responsible for the temperature anomalies caused by changing grid res-
 494 olution or dycore, as asserted above. In the deep Tropics, gravity waves are expected to
 495 propagate temperature anomalies far from their heating source, and so the misalignment
 496 is less troublesome for this region. In the mid-latitudes, we speculate that this misalign-
 497 ment is due to averaging the CLUBB heating over all time. Herrington and Reed (2020)
 498 have shown that only the CLUBB heating coinciding with upward resolved vertical ve-
 499 locities tends to align spatially with the temperature response, whereas heating anom-
 500 alies associated with descending grid columns had no alignment with the temperature re-
 501 sponse. Therefore the average over all time will dilute the heating signal, and potentially
 502 lead to misalignments between the heating rates and temperature anomalies.

503 Figure 5c shows that the **Arctic–GrIS** grid is much warmer than the **Arctic** grid
 504 in the Arctic summer. This may be due, in part, to the shorter physics time step, but
 505 the temperature response is too large to be explained by enhanced condensational heat-
 506 ing from CLUBB alone. This summer warming appears to be a result of variations in
 507 the stationary wave pattern, with a swath of anomalous southerly winds to the west of
 508 Greenland (not shown). This dynamic response is interesting, because other than the
 509 physics time step, the only difference between the **Arctic – GrIS** and **Arctic** runs is
 510 the doubling of resolution over Greenland. This behavior will be explored further in a
 511 future study.

512 Keeping our focus on the Arctic region, and in particular Greenland, it is useful
 513 to understand summer temperature biases due to their control on ice and snow melt over
 514 the GrIS (Ohmura, 2001). Figure 6 shows the 1979–1998 lower troposphere summer tem-
 515 perature bias relative to ERA5, computed by equating a layer mean virtual temperature
 516 with the 500–1000 hPa geopotential thickness. The results are consistent with the zonal
 517 mean height plots; increasing resolution from f19 to f09 warms the climate, and the 1°
 518 SE grids are warmer than the FV grids. The FV summer temperatures are persistently
 519 colder than ERA5, whereas the 1° SE grids are not as cold, and are actually warmer than
 520 ERA5 at high-latitudes, north of 75°. All grids show a north-south gradient in bias over
 521 Greenland, with the summer temperature bias more positive for the northern part of the
 522 ice sheet. This pattern is also evident in the near surface temperature bias over Green-
 523 land (not shown).

524 The **Arctic** grid has summer temperatures similar to the 1° SE grids, but is slightly
 525 warmer over northern Eurasia and the North Pole (Figure 6). An anomalous cooling patch
 526 forms to the west of Greenland, centered over Baffin Island. The **Arctic – GrIS** grid
 527 is warmer than the **Arctic** grid over most of the Arctic, but with a similar spatial pat-
 528 tern of summer temperature bias.

529 Some of these temperature differences may be related to differences in summer cloudi-
 530 ness. Figure 7 shows the summer shortwave cloud forcing bias in the six runs, using the
 531 CERES product. Shortwave cloud forcing quantifies the impact of clouds on shortwave
 532 radiation, taken as the difference between all-sky and clear-sky shortwave radiative fluxes
 533 at the top of the atmosphere. A negative bias corresponds to excessive reflection and cool-
 534 ing. The **lat-lon** and **quasi-uniform** grids have similar biases, with the clouds reflecting
 535 20–40 W/m² too much shortwave radiation over a wide swath of the Arctic, primarily
 536 the land masses. There is also a halo of positive bias (clouds not reflective enough) around
 537 the ocean perimeter of Greenland. The **Arctic** grid has much smaller cloud forcing bi-

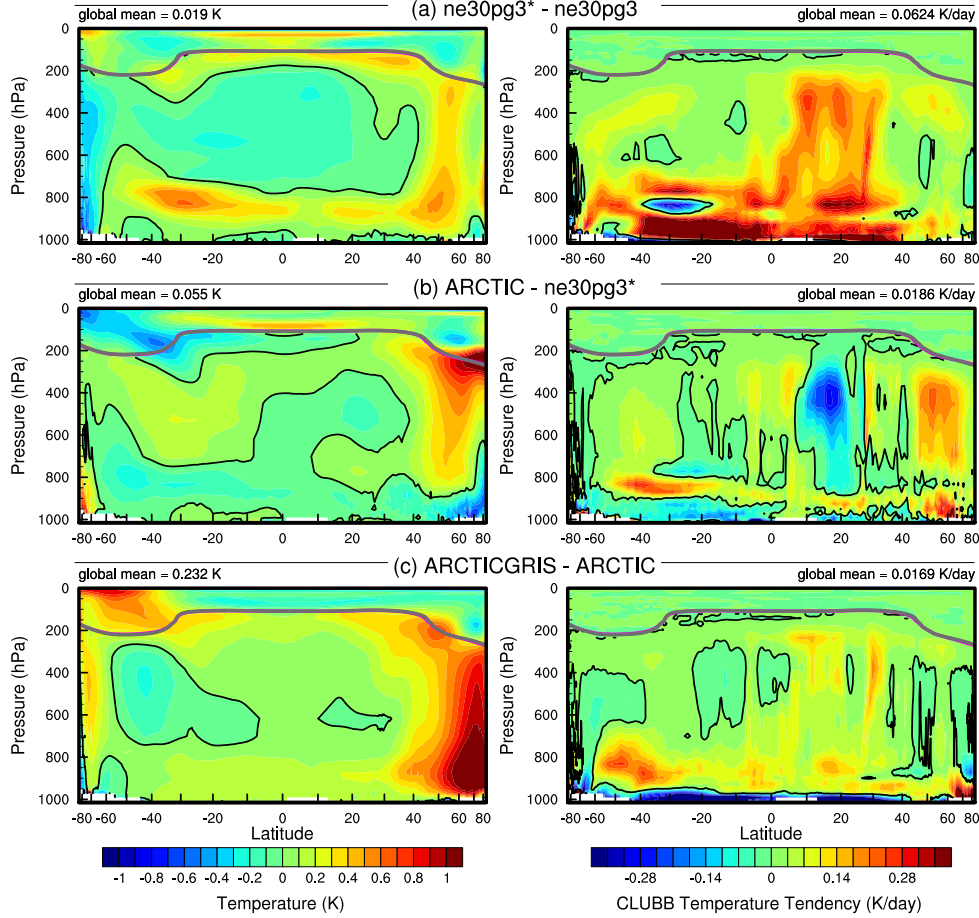


Figure 5. As in Figure 4 but for the short-time-step experiment and the VR grids. The fields plotted are for the climatological northern hemisphere summer. We focus on summer because that is when the resolution response is largest, and the refined regions are located in the northern hemisphere.

ases over the Arctic land masses, but is still too reflective over Alaska, the Canadian Archipelago, and parts of Eurasia. Compared to the **Arctic** grid, the **Arctic-GrIS** grid vastly reduces the cloud forcing bias over Eurasia, and also improves the bias over North America. In both VR grids, the halo of positive shortwave cloud forcing bias around the perimeter of Greenland is absent.

The summer cloud forcing biases are consistent with the summer temperature biases in Figure 6 – regions where clouds are too reflective coincide with regions that are too cold. While we have not quantified the contribution of cloud biases to the cooler Arctic temperatures, shortwave radiation is a crucial component of the Arctic energy budget during summer. The shortwave cloud forcing biases are on the order of 10 W/m², which is a significant fraction of the total absorbed shortwave **radiation** during Arctic summer (Serreze et al., 2007) and is therefore likely a factor contributing to the cooler temperatures.

grid name	accumulation	total melt	runoff	sublimation	SMB
RACMO	681.7 (733.5)	-318.6 (-436.4)	-189.1 (-258.5)	-34.5 (-38.8)	458.1 (436.2)
ne30pg2	1007. (973.4)	-519.9 (-647.3)	-381.9 (-347.0)	-33.9 (-32.1)	591.2 (594.3)
ne30pg3	931.0 (909.3)	-540.8 (-686.7)	-375.8 (-330.1)	-34.1 (-32.6)	521.2 (546.6)
f19	884.9 (913.5)	-414.0 (-546.5)	-284.0 (-284.3)	-36.5 (-37.5)	564.4 (591.7)
f09	873.9 (882.1)	-389.1 (-482.3)	-256.1 (-212.3)	-37.3 (-37.4)	580.5 (632.4)
Arctic	784.1 (818.6)	-335.5 (-436.8)	-215.8 (-194.2)	-42.4 (-43.9)	526.0 (580.5)
Arctic – GrIS	693.8 (747.3)	-437.3 (-610.4)	-276.8 (-307.8)	-48.1 (-51.8)	369.0 (387.7)

Table 3. 1979-1998 surface mass balance of the Greenland Ice Sheet in Gt/yr. Values shown are using the common ice mask approach described in the methods section, whereas values in parentheses are from integrating over the native grid and ice mask.

3.2 Clouds and precipitation over Greenland

In addition to summer temperatures, shortwave radiation is an important determinant of snow and ice melt. Figure 8 shows the summer incident shortwave radiation bias at the surface over Greenland and surrounding seas. The top panel shows the bias relative to the RACMO2.3p2 dataset, and the middle panel relative to the CERES dataset. The halo of excessive incident shortwave radiation around the coasts of Greenland is apparent for both datasets in relation to the coarser grids, consistent with the shortwave cloud forcing biases in Figure 7.

The ice sheet interior receives too little shortwave radiation in the coarser grids. On the VR grids, both the interior shortwave deficit and the excessive shortwave around the ocean perimeter are improved. This suggests that the coarse grid clouds are too thick in the interior of Greenland and too thin around the perimeter, which is consistent with the total summer cloud fraction bias, computed from the CALIPSO cloud dataset and shown in the bottom panel of Figure 8. Note that total cloud fraction characterizes the cloud field at all vertical levels, and attenuates the changes arising from any single layer due to the occurrence of overlapping clouds at other levels. The VR grids exhibit an overall improvement in total cloud fraction bias, relative to the coarse grids.

The top panel of Figure 9 shows the annual climatological mean precipitation bias over the GrIS, expressed as the fractional difference from the RACMO2.3p2 solution. The coarse $1^\circ - 2^\circ$ grids have large, positive biases centered over the southern dome. The Arctic grid reduces this bias substantially, and the Arctic–GrIS grid reduces it further, with precipitation centers migrating from the interior toward the margins.

The more accurate representation of orographic precipitation in the VR grids is consistent with the cloud and radiation biases, cf. Figures 7, 8, and 9. The agreement of the cloud, radiation and precipitation biases in and around Greenland from multiple independent datasets indicates that the biases are a robust feature of the coarser grids. The reduced biases in the VR grids suggest that the deficiencies of the coarse grids are due to insufficient horizontal resolution, consistent with previous findings that coarse GCMs have large, positive precipitation biases over Greenland (Pollard & Groups, 2000; Van Kamphout et al., 2019).

3.3 Greenland surface mass balance

Table 3 shows the 1979-1998 climatological SMB components for each grid, compared with RACMO. The values in the table are averages over the ensemble of mapping methods to the common ice masks described in section 2.7, and the RACMO values refer to the average of both RACMO ensembles. Table 3 also contains (in parenthesis) the SMB components derived from evaluating the integrals on each model’s native grid and

587 ice mask. Of note is the large reduction in melt rates compared to the values computed
 588 on the native grid, illustrating the dissipation of this quantity discussed in section 2.7.
 589 For integrated precipitation, the differences between the native and common ice mask
 590 approaches are much smaller, since the combined solid/liquid precipitation rates are not
 591 directly tied to the ice mask.

592 The coarse grids are characterized by too much precipitation and too much melt-
 593 ing and runoff, compared with RACMO. The total SMB on coarse grids therefore has
 594 smaller errors than the individual components (Table 3), because large errors in the source
 595 and sink terms offset one another when added together. Such compensating errors **underline**
 596 the importance of understanding the extent to which a model is getting the right
 597 SMB for the right reasons.

598 Figure 10 shows time series of annually integrated precipitation and snow/ice melt
 599 over the GrIS for the various different grids and dycores, and RACMO in black. The 1979-
 600 1998 climatological mean values from Table 3 are shown as circles on the right side of
 601 the panels. The **1°–2° lat-lon and quasi-uniform** grids have positive precipitation bi-
 602 ases, whereas the VR grids have the smallest biases, with precipitation comparable to
 603 RACMO. The f19 and f09 grids perform similarly, with +110 Gt/yr bias, whereas ne30pg3
 604 is biased by about +165 Gt/yr and ne30pg2 by +230 Gt/yr.

605 The combined annual snow/ice melt shown in the bottom panel of Figure 10 in-
 606 dicates that the **Arctic** grid simulates the most realistic melt rates, with the other grids
 607 having more melt than RACMO. The **Arctic–GrIS** grid over-predicts melting by about
 608 125 Gt/yr. This is likely due to an anomalously warm lower troposphere during the sum-
 609 mer, relative to the **Arctic** run (Figure 6). The f19 and f09 melting rates are improved
 610 over **Arctic–GrIS**, overestimating melt by only 70–90 Gt/yr. The SE grids have the
 611 largest positive melt bias, between 200–220 Gt/yr.

612 To illustrate the regional behavior of the SMB components, Figure 11 shows the
 613 precipitation and combined snow/ice melt integrated over the basins defined by Rignot
 614 and Mouginot (2012). The uncertainty due to differences in basin area is larger than for
 615 GrIS-wide integrals, owing to the differences in basin boundaries on the common ice masks,
 616 which are shown in the f19 and ne30pg2 panels of Figure 9. Nonetheless, the regional
 617 totals in Figure 11 correctly show the southeast and southwest basins have the most ac-
 618 cumulation. In all basins, accumulation decreases monotonically with increasing grid res-
 619 olution, though with some exceptions. The **Arctic–GrIS** grid simulates less precipi-
 620 tation than RACMO in the central-east and southeast basins, and is closest of all grids
 621 to RACMO in the large southwest basin.

622 The basin-integrated melt rates in Figure 11 depend on the dycore. The **quasi-uniform**
 623 SE grids have the largest positive biases in all basins. The **Arctic–GrIS** grid is a close
 624 second, while the FV grids have systematically **smaller melt-rates and melt-rate biases**.
 625 The “second-place” standing of **Arctic–GrIS** is somewhat unexpected, as this grid has
 626 the warmest lower-troposphere summer temperatures (Figure 6) and greatest incident
 627 shortwave radiation (Figure 8), yet it has less melting than the quasi-uniform SE grids.

628 Lower troposphere temperature is not a strict proxy for melting; e.g., it may not
 629 capture microclimate effects as a result of a better representation of the low-elevation
 630 ablation zones. The Positive Degree-Day temperature-based melt index (PDD; Braith-
 631 waite, 1984), which accumulates the near-surface temperature in °C for days with tem-
 632 perature above freezing, is a more accurate proxy for melting. PDD is nonlinear in mean
 633 monthly temperature (Reeh, 1991). We compute PDD from monthly mean 2-meter tem-
 634 perature using the method of Calov and Greve (2005), assuming a fixed monthly mean
 635 standard deviation of 3°C and a degree-day factor of 5 mm d⁻¹ °C⁻¹. **This specific degree-**
 636 **day factor lies between typical values reported for snow and ice, in order to easily ap-**
 637 **ply the PDD method to estimate the combined snow and ice melt.**

638 Figure 11c shows the basin-integrated PDD melt estimate. In the large southeast
 639 and southwest basins (and all the other western basins), the `ne30pg3` grid has larger PDD-
 640 based melt than the `Arctic-GrIS` grid. The FV grids also have large PDD-based melt
 641 in the southwest basin, relative to `Arctic-GrIS`. The PDD plots indicate that the re-
 642 lationship between temperature and melt is not well approximated by the summer lower-
 643 troposphere temperatures in Figure 6.

644 The bottom panel of Figure 9 presents the biases in the combined ice/snow melt
 645 as map plots. These plots show that the largest melt biases are on the southeast and north-
 646 west coasts, where large coarse-grid cells overlap with the ocean. One possibility is that
 647 these problematic grid cells are situated at lower elevations than the true ice sheet sur-
 648 face, leading to a warm bias and too much melt. Figure 12 shows the representation of
 649 the ice sheet surface along two transects on the different grids, compared to the high-
 650 resolution dataset used to generate CAM topographic boundary conditions (J. Daniel-
 651 son & Gesch, 2011; Lauritzen et al., 2015). The two transects are shown in Figure 9: the
 652 east-west “K-transsect” in southwest Greenland and a transect extending from the cen-
 653 tral dome down to the Kangerlussuaq glacier on the southeast coast. The `f09`
 654 grid is a bit of an exception since the grid cells narrow in the zonal direction at high lat-
 655 itudes, and so a larger number of grid cells fit into the east-west transects. The VR grids
 656 more accurately reproduce the steep margins of the ice sheet, capturing the character-
 657 istic parabolic shape of the GrIS margin.

659 The transects in Figure 12 show that the ice sheet surface on the coarse grids is
 660 not systematically lower than the true surface in ablation zones. Rather, the smooth-
 661 ing and flattening of the raw topography, necessary to prevent the model from exciting
 662 grid-scale numerical modes, causes the lower-elevation ablation zones to extend beyond
 663 the true ice sheet margin, causing the modeled ablation zones (which must reside within
 664 the ice sheet mask) to be elevated relative to the actual ice surface. The `f19` grid has
 665 both the smoothest topography and the flattest ice sheet since its dynamics are coars-
 666 est, whereas the `f09`, `ne30pg2` and `ne30pg3` grids have similar dynamical resolution and
 667 use identical smoothing. This suggests that coarser models will tend to elevate the ab-
 668 lation zones [relative to where they should be, which may be expected to cause anomalous \(adiabatic\) cooling and](#) depressed melt rates, but this is opposite the melt bias that
 669 occurs in the coarse grid simulations. [Also, the EC downscaling should be able to cor-](#)
 670 rect for situations where model ice surface is elevated relative to the true ice surface, al-
 671 though for very large elevation differences/errors the EC scheme may not be adequate.

673 Figure 12 also shows the ice margin boundary, illustrating that the ablation zone
 674 lies in a narrow horizontal band where the ice sheet rapidly plunges to sea-level. Due to
 675 this abrupt transition, coarse grids will commonly represent the ablation zone with grid
 676 cells containing mixtures of ice-covered and ice-free regions. We hypothesize that coarser
 677 models have larger melt biases because summer melting is confined to these mixed ice/land/ocean
 678 grid cells. CLM deals with land heterogeneity in a complex and sophisticated manner,
 679 but CAM only sees the homogenized state after [area](#) averaging over the sub-grid mix-
 680 ture. Thus, warm ice-free land patches in a grid cell may unduly influence the climate
 681 over the entire grid cell, causing a warm bias over the ice-covered patch [and more melt-
 682 ing.](#)

683 Figure 13 shows the mean melt bias, relative to both RACMO datasets, condition-
 684 ally sampled based on grid cell ice fraction in the GrIS region. Errors are computed af-
 685 ter mapping the melt rates to the common ice masks using different methods, described
 686 in section 2.7. The grid cell ice fractions therefore pertain to ice fractions on the low-
 687 resolution common ice masks. Also shown are the ± 1 standard deviation of the biases
 688 for each bin. The figure shows that coarser grids can be characterized by a monotonic
 689 increase in melt bias as the grid cell ice fraction decreases. The VR grids have the small-
 690 est melt biases for small grid cell ice fractions (less than 50%), the [quasi-uniform SE](#) grids

and **f19** have the largest melt biases and the **f09** grid melt biases lie between these two cases. Figure 13 generally supports our hypothesis that the prevalence of mixed-grid cells in the ablation zone of coarse grids is responsible for their large melt bias.

Another potential factor in explaining the melt differences across the grids and dycores is the surface albedo. Bare ice has a lower albedo than snow, so it's reasonable to speculate whether the large melt biases in the coarse grid simulations are in part due to more frequent bare ice exposure. One reasonable pathway to more bare ice exposure is related to the precipitation and cloud biases. As the lat-lon and quasi-uniform grids accumulate too much precipitation in the GrIS interior, it's possible the coastal ice margins receive too little snow, which may be more easily melted away to expose the underlying glacial ice. The top row of Figure 14 shows the summer snow cover bias relative to ERA5. There is no indication that the coastal regions have lower snow fractions, and more bare ice exposure, compared with the VR runs. In southeast Greenland, the coarse runs have anomalously high snow cover relative to the VR runs. In southwest and central-west Greenland, the snow cover is anomalously low, but arguably no more so than occurs in the VR runs. And in combining these results with the precipitation biases (Figure 13), there just isn't much support for a reduction in snowfall and snow cover around the coastal margins in the coarser runs.

The middle and bottom rows of Figure 14 show maps of summer albedo biases in the simulations, relative to the RACMO2.3p2 and the processed MODIS albedo dataset of Tedesco and Alexander (2013). The model surface albedo is diagnosed from the incident and net shortwave radiative fluxes at the surface. While RACMO2.3p2 indicates that the albedo near the southwest/southeast coastal margins is lower in the lat-lon and quasi-uniform grids relative to the VR grids, the MODIS dataset does not show that the VR grids have a substantially different albedo from the coarse grids. We do observe a persistent positive albedo bias in the northwest in all grids, in both validation datasets, which is consistent with a low melt bias in that region (Lofverstrom et al., 2020).

3.4 Precipitation extremes

Synoptic storms are tracked using TempestExtremes atmospheric feature detection software (Ullrich et al., 2021). As the **Arctic** grid contains $1/4^\circ$ refinement north of about 45° latitude, the storm tracker is applied to this region for the **Arctic** and **ne30pg3** runs to identify differences in storm characteristics due to horizontal resolution.

Figure 15 shows monthly PDF (probability density function) of the precipitation rates associated with storms. The PDFs are constructed by sampling all the precipitation rates within 30° of the storm center, for each point on the storm track and for all storms. The PDFs are evaluated on an identical composite grid for all runs, and so storm statistics are not impacted by differences in output resolution. The **Arctic** run has larger extreme precipitation rates compared to **ne30pg3** in every month, but the increase is greatest in the summer months, which coincides with the most extreme events of the year. This is primarily due to increased resolution and not the reduced physics time step; the **ne30pg3*** run only marginally increases the extreme precipitation rates compared with **ne30pg3** (Figure 15).

The extreme precipitation rates in the **Arctic** run are closer than **ne30pg3** to the ERA5 reanalysis (Figure 15). It is difficult to know how much the extreme precipitation rates in ERA5 are constrained by data assimilation, or whether these precipitation rates are due to using a similar $1/4^\circ$ model as the **Arctic** grid. However, it is well documented that $1/4^\circ$ models are more skillful at simulating extreme events (Bacmeister et al., 2013; Obrien et al., 2016). A more realistic representation of extreme precipitation events is an additional benefit of the VR grids.

740 4 Conclusions

741 Running CESM2.2 in an AMIP-style configuration, we have evaluated six grids from
 742 two dynamical cores for their performance over the Arctic and in simulating the GrIS
 743 SMB. The $1 - 2^\circ$ finite-volume grids have enhanced resolution over polar regions due
 744 to their convergence of meridian lines, although a polar filter is used to prevent spuri-
 745 ous atmospheric features from forming in these regions. SE grids comparable to the res-
 746 olution of the FV grids have an isotropic grid structure where the grid resolution is sim-
 747 ilar over the entire model domain. We developed two VR grids and introduced them into
 748 CESM2.2 as part of this work. Both use the SE dycore; the **Arctic** grid has $1/4^\circ$ refine-
 749 ment over the broader Arctic, whereas the **Arctic – GrIS** grid is identical except for
 750 a $1/8^\circ$ patch of refinement over Greenland. A third VR grid, **CONUS**, with $1/8^\circ$ refine-
 751 ment over the **US**, has also been made available in CESM2.2.

752 In general, the FV grids have colder summer temperatures over the Arctic com-
 753 pared with the SE grids (including the VR grids). The cloud biases in all the **lat-lon and**
 754 **quasi-uniform** resolution grids, whether FV or SE, are similar, in general being too cloudy
 755 over Arctic land masses. It should be emphasized that our analysis is specific to the Arc-
 756 tic summer because of its relevance to GrIS melt rates. An improved representation of
 757 clouds in the Arctic does not imply improved clouds at lower latitudes.

758 At the regional level, there is a halo of negative cloudiness bias around the ocean
 759 perimeter of Greenland on all $1 - 2^\circ$ grids, but not the VR grids. This negative cloud
 760 bias contrasts with a positive cloud bias over the ice sheet interior. This anomaly pat-
 761 tern is attributed to deficient orographic precipitation in the coarser model grids. With
 762 overly smooth topography on the $1 - 2^\circ$ grids, synoptic systems moving into Greenland
 763 are not sufficiently lifted when encountering the steep ice margins. As a result, excess
 764 precipitation falls in the GrIS interior, instead of being concentrated on the steep coastal
 765 margins as shown by observations (Pollard & Groups, 2000; Van Kampenhout et al., 2019).
 766 This results in a positive precipitation and cloud bias in the ice sheet interior, and a halo
 767 of low cloud bias about the perimeter. The agreement of different observational data prod-
 768 ucts on this bias lends confidence in the attribution of causes. The VR grids compare
 769 better to the observations and show that orographic precipitation in Greenland is largely
 770 resolved when the horizontal resolution is increased sufficiently.

771 We integrated the primary source and sink terms of the SMB equation over the GrIS
 772 for each of the six grids. The **$1^\circ - 2^\circ$ lat-lon and quasi-uniform** grids have large posi-
 773 tive accumulation biases because they fail to resolve orographic precipitation. The quasi-
 774 uniform SE grids have larger accumulation biases, suggesting that the FV grids are more
 775 skillful for precipitation due to finer resolution over Greenland, and despite a polar fil-
 776 ter. The VR grids have the most accurate accumulation rates of all the grids. The pri-
 777 mary mass sink term of the GrIS, ice/snow melt, has similar biases; the coarse grids melt
 778 too much, with a greater bias for quasi-uniform SE grids. In general, on coarse grids, er-
 779 rors in the individual SMB terms are larger than the errors in the SMB itself, due to com-
 780 pensating errors. This observation serves as a precaution; projecting mass-loss from a
 781 glacier or ice sheet cannot be reliable if the processes representing the components of the
 782 SMB are incorrect from the start, even if the total SMB has the right magnitude.

783 The **Arctic – GrIS** grid has the warmest summer lower troposphere of all grids,
 784 yet it has less melting than the quasi-uniform resolution SE grids. This suggests that
 785 grid resolution is somehow contributing to the melt biases in coarse grids, in a way that
 786 is not obvious from the large-scale dynamics. We propose a mechanism: coarse grids rep-
 787 resent ablation zones using grid cells with mixed surface types, ice-covered and ice-free.
 788 The warmer ice-free patches may largely determine the mean state, leading to a warm
 789 bias over the ice-covered patches of the grid cell. This mechanism is supported by anal-
 790 ysis of melt biases binned by grid-cell ice fraction, **although further testing of this hy-**
 791 **pothesis is needed.**

The Arctic grid substantially improves the simulated Arctic climate, including precipitation extremes and the GrIS SMB, compared to the 1°–2° lat-lon and quasi-uniform grids. The Arctic–GrIS grid has the most realistic cloud and precipitation fields, but its summer temperatures are too warm. The 1° FV model gives a surprisingly realistic SMB, likely due to the relatively fine resolution of Greenland on lat-lon grids (but perhaps also because it is the most heavily tuned model configuration in CESM). In particular, a greater number of grid cells in the ablation zone reduces the influence of mixed ice-covered/ice-free grid cells that represent ablation poorly on the other lat-lon and quasi-uniform grids.

As modeling systems move away from lat-lon grids towards quasi-uniform unstructured grids, it is worth taking stock of whether this will degrade the simulated polar climate. We have found that the 1° FV model has clear advantages over the 1° SE model for simulating the GrIS SMB. The SE dycore is still under active development (e.g., Appendix A) compared to the more mature FV dycore, and future algorithmic improvements may reduce the FV-SE GrIS SMB skill gap. However, such developments are unlikely to eliminate this skill gap entirely due to the fewer number of grid cells representing high latitude structures on quasi-uniform unstructured grids. The simulated GrIS SMB will be adversely impacted in future CESM versions, after the FV dycore is phased out. This finding will not interrupt the ongoing transition towards unstructured grids in CESM, which is largely driven by gains in computational efficiency and grid refinement capabilities. We therefore provide the Arctic refined-meshes to the community by way of CESM2.2, providing users the option to simulate a more realistic GrIS SMB, although at a substantial computational premium relative to conventional 1°–2° grids.

We are working to develop a configuration of the Arctic grid that is fully-coupled with the CESM ocean and sea ice components and the Community Ice Sheet Model (CISM), to provide multi-century projections of the state of the GrIS and its contribution to sea-level rise. We have also developed a visualization of the Arctic–GrIS run, now available on youtube (see link in Acknowledgements) to increase awareness of the capabilities of CESM2.2. Figure 16 shows a snapshot of this visualization, illustrating mesoscale katabatic winds descending the southeastern slopes of the GrIS. These new grids and configurations will provide new opportunities for CESM polar science, and they aim to contribute to an improved understanding of the polar environment. However, we recognize the potentially prohibitive costs for some users, and so will continue to explore different grids, parameterizations and workflows that can provide some of the same benefits of the VR grids, but at a lower cost.

Appendix A Details on spectral-element dynamical core improvements since the CESM2.0 release

Since the CESM2.0 release of the spectral-element dynamical core documented in Lauritzen et al. (2018) some important algorithmic improvements have been implemented and released with CESM2.2. These pertain mainly to the flow over orography that, for the spectral-element dynamical core, can lead to noise aligned with the element boundaries (Herrington et al., 2018).

A1 Reference profiles

Significant improvement in removing noise for flow over orography can be achieved by using reference profiles for temperature and pressure

$$T^{(ref)} = T_0 + T_1 \Pi^{(ref)}, \quad (\text{A1})$$

$$p_s^{(ref)} = p_0 \exp\left(-\frac{\Phi_s}{R^{(d)} T_{ref}}\right), \quad (\text{A2})$$

(Simmons & Jiabin, 1991) where $T_1 = \Gamma_0 T_{ref} c_p^{(d)} / g \approx 192K$, with gravity g , and standard lapse rate $\Gamma_0 \equiv 6.5K/km$ and $T_0 \equiv T_{ref} - T_1 \approx 97K$; $T_{ref} = 288K$ ($c_p^{(d)}$ specific heat of dry air at constant pressure; $R^{(d)}$ gas constant for dry air), and Φ_s is the surface geopotential. The reference Exner function is

$$\Pi^{(ref)} = \left(\frac{p^{(ref)}}{p_0} \right)^\kappa \quad (\text{A3})$$

where $\kappa = \frac{R^{(d)}}{c_p^{(d)}}$. The reference surface pressure $p_0 = 1000hPa$ and at each model level the reference pressure $p^{(ref)}$ is computed from $p_s^{(ref)}$ and the standard hybrid coefficients

$$p^{(ref)}(\eta) = A(\eta)p_0 + B(\eta)p_s^{(ref)}, \quad (\text{A4})$$

where A and B are the standard hybrid coefficients (using a dry-mass generalized vertical mass coordinate η). These reference profiles are subtracted from the prognostic temperature and pressure-level-thickness states before applying hyperviscosity:

CESM2.0 → CESM2.2

$$\nabla_\eta^4 T \rightarrow \nabla_\eta^4 (T - T^{(ref)}), \quad (\text{A5})$$

$$\nabla_\eta^4 \delta p^{(d)} \rightarrow \nabla_\eta^4 (\delta p^{(d)} - \delta p^{(ref)}). \quad (\text{A6})$$

This reduces spurious transport of temperature and mass up/down-slope due to the hyperviscosity operator.

A2 Rewriting the pressure gradient force (PGF)

In the CESM2.0 the following (standard) form of the pressure gradient term was used:

$$\nabla_\eta \Phi + \frac{1}{\rho} \nabla_\eta p, \quad (\text{A7})$$

where Φ is geopotential and $\rho = \frac{R^{(d)} T_v}{p}$ is density (for details see Lauritzen et al., 2018). To alleviate noise for flow over orography, we switched to an Exner pressure formulation following Taylor et al. (2020), which uses that (A7) can be written in terms of the Exner pressure

$$\nabla_\eta \Phi + c_p^{(d)} \theta_v \nabla_\eta \Pi, \quad (\text{A8})$$

where the Exner pressure is

$$\Pi \equiv \left(\frac{p}{p_0} \right)^\kappa. \quad (\text{A9})$$

and virtual temperature is

$$T_v = T \left(\frac{1 + \frac{1}{\epsilon} m^{(wv)}}{\sum_{\ell \in \mathcal{L}_{all}} m^{(\ell)}} \right), \quad (\text{A10})$$

where $m^{(\ell)}$ is dry mixing ratio of component of moist air ℓ ; \mathcal{L}_{all} is the set of all components of moist air and, in particular, ' wv ' is water vapor.

The derivation showing that (A7) and (A8) are equivalent is given here:

$$\begin{aligned} c_p^{(d)} \theta_v \nabla_\eta \Pi &= c_p^{(d)} \theta_v \nabla_\eta \left(\frac{p}{p_0} \right)^\kappa, \\ &= c_p^{(d)} \theta_v \kappa \left(\frac{p}{p_0} \right)^{\kappa-1} \nabla_\eta \left(\frac{p}{p_0} \right), \\ &= c_p^{(d)} \theta_v \kappa \Pi \left(\frac{p_0}{p} \right) \nabla_\eta \left(\frac{p}{p_0} \right), \end{aligned}$$

$$\begin{aligned}
&= \frac{c_p^{(d)} \theta_v \kappa \Pi}{p} \nabla_\eta p, \\
&= \frac{R^{(d)} \theta_v \Pi}{p} \nabla_\eta p, \\
&= \frac{R^{(d)} T_v}{p} \nabla_\eta p, \\
&= \frac{1}{\rho} \nabla_\eta p.
\end{aligned}$$

where virtual potential temperature is T_v/Π . Using the reference states from (Simmons & Jiabin, 1991),

$$\bar{T} = T_0 + T_1 \Pi, \quad (\text{A11})$$

$$\bar{\theta} = T_0/\Pi + T_1, \quad (\text{A12})$$

we can define a geopotential as a function of Exner pressure

$$\bar{\Phi} = -c_p^{(d)} (T_0 \log \Pi + T_1 \Pi - T_1). \quad (\text{A13})$$

This "balanced" geopotential obeys

$$c_p^{(d)} \bar{\theta} \nabla \Pi + \nabla \bar{\Phi} = 0 \quad (\text{A14})$$

for any Exner pressure. Subtracting this "reference" profile from the PGF yields

$$\begin{aligned}
\nabla_\eta \Phi + c_p^{(d)} \theta_v \nabla_\eta \Pi &= \nabla_\eta (\Phi - \bar{\Phi}) + c_p^{(d)} (\theta_v - \bar{\theta}) \nabla_\eta \Pi, \\
&= \nabla_\eta \Phi + c_p^{(d)} \theta_v \nabla_\eta \Pi + c_p^{(d)} T_0 \left[\nabla_\eta \log \Pi - \frac{1}{\Pi} \nabla_\eta \Pi \right]. \quad (\text{A15})
\end{aligned}$$

In the continuum, the two formulations (left and right-hand side of (A15)) are identical. But under discretization, the second formulation can have much less truncation error.

A3 Results

One year averages of vertical pressure velocity at 500hPa (OMEGA500) have been found to be a useful quantity to detect spurious up or down-drafts induced by steep orography (Figure A1). While the true solution is not known, strong vertical velocities aligned with element edges that are not found in the CAM-FV reference solution (Figure A1(a)) are likely not physical (spurious). The older CESM2.0 version of SE (Figure A1(d)) using the "traditional" discretization of the PGF, (A15), exhibits significant spurious noise patterns around steep orography compared to CAM-FV (e.g., around Himalayas and Andes). This is strongly alleviated by switching to the Exner formulation of the PGF (A8; Figure A1(c)). By also subtracting reference profiles from pressure-level thickness and temperature, equations (A5) and (A6) respectively, reduces strong up-down drafts further (Figure A1(d)). Switching to the CAM-SE-CSLAM version where physics tendencies are computed on an quasi-equal area physics grid and using the CSLAM transport scheme, marginal improvements are observed in terms of a smoother vertical velocity field (Figure A1(e,f)). The configuration shown in Figure A1(d) is used for the simulations shown in the main text of this paper.

It is interesting to note that the noise issues and algorithmic remedies found in the real-world simulations discussed above, can be investigated by replacing all of physics with a modified version of the Held-Suarez forcing (Held & Suarez, 1994). The original formulation of the Held-Suarez idealized test case used a flat Earth ($\Phi_s = 0$) and a dry atmosphere. By simply adding the surface topography used in 'real-world' simulations and removing the temperature relaxation in the lower part of domain ($\sigma > 0.7$; see Held

890 and Suarez (1994) for details), surprisingly realistic vertical velocity fields (in terms of
 891 structure) result (see Figure A2). Since this was a very useful development tool it is shared
 892 in this manuscript.

893 Acknowledgments

894 This material is based upon work supported by the National Center for Atmospheric Re-
 895 search (NCAR), which is a major facility sponsored by the NSF under Cooperative Agree-
 896 ment 1852977. Computing and data storage resources, including the Cheyenne super-
 897 computer (Computational and Information Systems Laboratory, 2017), were provided
 898 by the Computational and Information Systems Laboratory (CISL) at NCAR. A. Her-
 899 rington thanks Matt Rehme (NCAR/CISL) for his role in generating the Arctic–GrIS
 900 visualization available on youtube (https://www.youtube.com/watch?v=YwHgqDu75s8&t=4s&ab_channel=NCARVisLab).

902 The data presented in main part of this manuscript is available at <https://github.com/adamrher/2020-arcticgrids>. The source code and data for the Appendix is avail-
 903 able at <https://github.com/PeterHjortLauritzen/CAM/tree/topo-mods>.
 904

905 References

- Alexander, P., LeGrande, A., Fischer, E., Tedesco, M., Fettweis, X., Kelley, M., ...
 906 Schmidt, G. (2019). Simulated greenland surface mass balance in the giss
 907 modele2 gcm: Role of the ice sheet surface. *Journal of Geophysical Research: Earth Surface*, 124(3), 750–765.
 908
 Bacmeister, J. T., Reed, K. A., Hannay, C., Lawrence, P., Bates, S., Truesdale,
 909 J. E., ... Levy, M. (2016). Projected changes in tropical cyclone activity un-
 910 der future warming scenarios using a high-resolution climate model. *Climatic
 911 Change*. doi: 10.1007/s10584-016-1750-x
 912
 Bacmeister, J. T., Wehner, M. F., Neale, R. B., Gettelman, A., Hannay, C., Lau-
 913 ritzen, P. H., ... Truesdale, J. E. (2013). Exploratory high-resolution climate
 914 simulations using the community atmosphere model (cam). *J. Climate*, 27(9),
 915 3073–3099. doi: 10.1175/JCLI-D-13-00387.1
 916
 Bambach, N. E., Rhoades, A. M., Hatchett, B. J., Jones, A. D., Ullrich, P. A., &
 917 Zarzycki, C. M. (2021). Projecting climate change in south america using
 918 variable-resolution community earth system model: An application to chile.
International Journal of Climatology.
 919
 Beljaars, A., Brown, A., & Wood, N. (2004). A new parametrization of turbulent
 920 orographic form drag. *Quart. J. Roy. Meteor. Soc.*, 130(599), 1327–1347. doi:
 921 10.1256/qj.03.73
 922
 Bogenschutz, P. A., Gettelman, A., Morrison, H., Larson, V. E., Craig, C., & Scha-
 923 nen, D. P. (2013). Higher-order turbulence closure and its impact on climate
 924 simulations in the community atmosphere model. *Journal of Climate*, 26(23),
 925 9655–9676.
 926
 Box, J. E., Bromwich, D. H., & Bai, L.-S. (2004). Greenland ice sheet surface mass
 927 balance 1991–2000: Application of polar mm5 mesoscale model and in situ
 928 data. *Journal of Geophysical Research: Atmospheres*, 109(D16).
 929
 Braithwaite, R. J. (1984). Calculation of degree-days for glacier-climate research.
Zeitschrift für Gletscherkunde und Glazialgeologie, 20(1984), 1–8.
 930
 Burakowski, E. A., Tawfik, A., Ouimette, A., Lepine, L., Zarzycki, C., Novick, K.,
 931 ... Bonan, G. (2019). Simulating surface energy fluxes using the variable-
 932 resolution community earth system model (vr-cesm). *Theoretical and Applied
 933 Climatology*, 138(1), 115–133.
 934
 Calov, R., & Greve, R. (2005). A semi-analytical solution for the positive degree-day
 935 model with stochastic temperature variations. *Journal of Glaciology*, 51(172),
 936 173–175.
 937
 938
 939

- 941 Canuto, C., Hussaini, M. Y., Quarteroni, A., & Zang, T. (2007). *Spectral methods:*
 942 *Evolution to complex geometries and applications to fluid dynamics* (1st ed.).
 943 Springer.
- 944 Chang, P., Zhang, S., Danabasoglu, G., Yeager, S. G., Fu, H., Wang, H., ... oth-
 945 ers (2020). An unprecedented set of high-resolution earth system simulations
 946 for understanding multiscale interactions in climate variability and change.
 947 *Journal of Advances in Modeling Earth Systems*, 12(12), e2020MS002298.
- 948 Chepfer, H., Bony, S., Winker, D., Cesana, G., Dufresne, J., Minnis, P., ... Zeng, S.
 949 (2010). The gcm-oriented calipso cloud product (calipso-goccp). *Journal of*
 950 *Geophysical Research: Atmospheres*, 115(D4).
- 951 Collins, W. D., Rasch, P. J., Boville, B. A., Hack, J. J., McCaa, J. R., Williamson,
 952 D. L., ... Zhang, M. (2006). The formulation and atmospheric simulation
 953 of the community atmosphere model version 3 (cam3). *Journal of Climate*,
 954 19(11), 2144–2161.
- 955 Computational and Information Systems Laboratory. (2017). *Cheyenne: HPE/SGI*
 956 *ICE XA System (Climate Simulation Laboratory)*, Boulder, CO: National
 957 Center for Atmospheric Research. doi: 10.5065/D6RX99HX
- 958 Copernicus, C. (2019). Era5 monthly averaged data on pressure levels from
 959 1979 to present. URL: <https://cds.climate.copernicus.eu>. doi: 10.24381/
 960 cds.6860a573
- 961 Craig, C., Bacmeister, J., Callaghan, P., Eaton, B., Gettelman, A., Goldhaber, S. N.,
 962 ... Vitt, F. M. (2021). *Cam6.3 user's guide* (Tech. Rep.). NCAR/TN-
 963 571+EDD. doi: 10.5065/Z953-ZC95
- 964 Danabasoglu, G., Lamarque, J.-F., Bacmeister, J., Bailey, D., DuVivier, A., Ed-
 965 wards, J., ... others (2020). The community earth system model ver-
 966 sion 2 (cesm2). *Journal of Advances in Modeling Earth Systems*, 12(2),
 967 e2019MS001916.
- 968 Danielson, J., & Gesch, D. (2011). *Global multi-resolution terrain elevation data*
 969 *2010 (GMTED2010)* (Open-File Report 2011-1073). U.S. Geological Survey.
 970 (<http://pubs.usgs.gov/of/2011/1073/pdf/of2011-1073.pdf>)
- 971 Danielson, J. J., & Gesch, D. B. (2011). *Global multi-resolution terrain elevation*
 972 *data 2010 (GMTED2010)* (Open File Rep. No. 2011-1073). US Geological Sur-
 973 vey. doi: <https://doi.org/10.3133/ofr20111073>
- 974 Dennis, J., Edwards, J., Evans, K. J., Guba, O., Lauritzen, P. H., Mirin, A. A., ...
 975 Worley, P. H. (2012). CAM-SE: A scalable spectral element dynamical core for
 976 the Community Atmosphere Model. *Int. J. High. Perform. C.*, 26(1), 74-89.
 977 Retrieved from <http://hpc.sagepub.com/content/26/1/74.abstract> doi:
 978 10.1177/1094342011428142
- 979 Dennis, J., Fournier, A., Spotz, W., St-Cyr, A., Taylor, M., Thomas, S., & Tufo, H.
 980 (2005). High-resolution mesh convergence properties and parallel efficiency
 981 of a spectral element atmospheric dynamical core. *ijhpc*, 19, 225-235. doi:
 982 10.1177/1094342005056108
- 983 Evans, K. J., Kennedy, J. H., Lu, D., Forrester, M. M., Price, S., Fyke, J., ... oth-
 984 ers (2019). Livvkit 2.1: automated and extensible ice sheet model validation.
 985 *Geoscientific Model Development*, 12(3), 1067–1086.
- 986 Eyring, V., Bony, S., Meehl, G. A., Senior, C. A., Stevens, B., Stouffer, R. J., &
 987 Taylor, K. E. (2016). Overview of the coupled model intercomparison project
 988 phase 6 (cmip6) experimental design and organization. *Geoscientific Model*
 989 *Development*, 9(5), 1937–1958.
- 990 Fettweis, X., Franco, B., Tedesco, M., Van Angelen, J., Lenaerts, J. T., van den
 991 Broeke, M. R., & Gallée, H. (2013). Estimating the greenland ice sheet
 992 surface mass balance contribution to future sea level rise using the regional
 993 atmospheric climate model mar. *The Cryosphere*, 7(2), 469–489.
- 994 Gettelman, A., Callaghan, P., Larson, V., Zarzycki, C., Bacmeister, J., Lauritzen, P.,
 995 ... Neale, R. (2017). Regional climate simulations with the community earth

- 996 system model. *J. Adv. Model. Earth Syst.*. (submitted)
- 997 Gettelman, A., Hannay, C., Bacmeister, J. T., Neale, R. B., Pendergrass, A., Dan-
998 abasoglu, G., ... others (2019). High climate sensitivity in the community
999 earth system model version 2 (cesm2). *Geophysical Research Letters*, 46(14),
1000 8329–8337.
- 1001 Gettelman, A., & Morrison, H. (2015). Advanced two-moment bulk microphysics for
1002 global models. part i: Off-line tests and comparison with other schemes. *Journal
1003 of Climate*, 28(3), 1268–1287.
- 1004 Gettelman, A., Morrison, H., Santos, S., Bogenschutz, P., & Caldwell, P. (2015).
1005 Advanced two-moment bulk microphysics for global models. part ii: Global
1006 model solutions and aerosol–cloud interactions. *Journal of Climate*, 28(3),
1007 1288–1307.
- 1008 Golaz, J.-C., Larson, V. E., & Cotton, W. R. (2002). A pdf-based model for bound-
1009 ary layer clouds. part i: Method and model description. *Journal of the Atmo-*
1010 *spheric Sciences*, 59(24), 3540–3551. doi: 10.1175/1520-0469(2002)059<3540:
1011 apbmfb>2.0.co;2
- 1012 Guba, O., Taylor, M. A., Ullrich, P. A., Overfelt, J. R., & Levy, M. N. (2014). The
1013 spectral element method (sem) on variable-resolution grids: evaluating grid
1014 sensitivity and resolution-aware numerical viscosity. *Geosci. Model Dev.*, 7(6),
1015 2803–2816. doi: 10.5194/gmd-7-2803-2014
- 1016 Guo, Z., Wang, M., Qian, Y., Larson, V. E., Ghan, S., Ovchinnikov, M., ... Zhou,
1017 T. (2015). Parametric behaviors of clubb in simulations of low clouds in the c
1018 ommunity atmosphere model (cam). *Journal of Advances in Modeling Earth
1019 Systems*, 7(3), 1005–1025.
- 1020 Hansen, N., Simonsen, S. B., Boberg, F., Kittel, C., Orr, A., Souverijns, N., ... Mot-
1021 tram, R. (2022). Brief communication: Impact of common ice mask in surface
1022 mass balance estimates over the antarctic ice sheet. *The Cryosphere*, 16(2),
1023 711–718.
- 1024 Held, I. M., & Suarez, M. J. (1994). A proposal for the intercomparison of the dy-
1025 namical cores of atmospheric general circulation models. *Bull. Am. Meteorol.
1026 Soc.*, 73, 1825–1830.
- 1027 Herrington, A. R., Lauritzen, P., Taylor, M. A., Goldhaber, S., Eaton, B. E.,
1028 Bacmeister, J., ... Ullrich, P. (2018). Physics-dynamics coupling with element-
1029 based high-order galerkin methods: quasi equal-area physics grid. *Mon. Wea.
1030 Rev.*, 47, 69–84. doi: 10.1175/MWR-D-18-0136.1
- 1031 Herrington, A. R., Lauritzen, P. H., Reed, K. A., Goldhaber, S., & Eaton, B. E.
1032 (2019). Exploring a lower resolution physics grid in cam-se-cslam. *Journal of
1033 Advances in Modeling Earth Systems*, 11.
- 1034 Herrington, A. R., & Reed, K. A. (2018). An idealized test of the response of the
1035 community atmosphere model to near-grid-scale forcing across hydrostatic
1036 resolutions. *J. Adv. Model. Earth Syst.*, 10(2), 560–575.
- 1037 Herrington, A. R., & Reed, K. A. (2020). On resolution sensitivity in the commu-
1038 nity atmosphere model. *Quarterly Journal of the Royal Meteorological Society*,
1039 146(733), 3789–3807.
- 1040 Hurrell, J. W., Hack, J. J., Shea, D., Caron, J. M., & Rosinski, J. (2008). A new
1041 sea surface temperature and sea ice boundary dataset for the community at-
1042 mosphere model. *Journal of Climate*, 21(19), 5145–5153.
- 1043 Jablonowski, C., & Williamson, D. L. (2011). The pros and cons of diffusion, fil-
1044 ters and fixers in atmospheric general circulation models. In P. H. Lauritzen,
1045 C. Jablonowski, M. Taylor, & R. Nair (Eds.), *Numerical techniques for global
1046 atmospheric models* (pp. 381–493). Berlin, Heidelberg: Springer Berlin Heidel-
1047 berg. doi: 10.1007/978-3-642-11640-7_13
- 1048 Lauritzen, P. H., Bacmeister, J. T., Callaghan, P. F., & Taylor, M. A. (2015).
1049 NCAR_Topo (v1.0): NCAR global model topography generation soft-
1050 ware for unstructured grids. *Geosci. Model Dev.*, 8(12), 3975–3986. doi:

- 1051 10.5194/gmd-8-3975-2015
- 1052 Lauritzen, P. H., Jablonowski, C., Taylor, M., & Nair, R. D. (2010). Rotated
1053 versions of the jablonowski steady-state and baroclinic wave test cases: A
1054 A dynamical core intercomparison. *J. Adv. Model. Earth Syst.*, 2(15), 34 pp.
- 1055 Lauritzen, P. H., Mirin, A., Truesdale, J., Raeder, K., Anderson, J., Bacmeister, J.,
1056 & Neale, R. B. (2011). Implementation of new diffusion/filtering operators
1057 in the CAM-FV dynamical core. *Int. J. High Perform. Comput. Appl.*. doi:
1058 10.1177/1094342011410088
- 1059 Lauritzen, P. H., Nair, R., Herrington, A., Callaghan, P., Goldhaber, S., Dennis, J.,
1060 ... Dubos, T. (2018). NCAR release of CAM-SE in CESM2.0: A reformula-
1061 tion of the spectral-element dynamical core in dry-mass vertical coordinates
1062 with comprehensive treatment of condensates and energy. *J. Adv. Model.*
1063 *Earth Syst.*, 10(7), 1537-1570. doi: 10.1029/2017MS001257
- 1064 Lauritzen, P. H., Taylor, M. A., Overfelt, J., Ullrich, P. A., Nair, R. D., Goldhaber,
1065 S., & Kelly, R. (2017). CAM-SE-CSLAM: Consistent coupling of a conser-
1066 vative semi-lagrangian finite-volume method with spectral element dynamics.
1067 *Mon. Wea. Rev.*, 145(3), 833-855. doi: 10.1175/MWR-D-16-0258.1
- 1068 Lawrence, D. M., Fisher, R. A., Koven, C. D., Oleson, K. W., Swenson, S. C., Bo-
1069 nan, G., ... others (2019). The community land model version 5: Description
1070 of new features, benchmarking, and impact of forcing uncertainty. *Journal of*
1071 *Advances in Modeling Earth Systems*, 11(12), 4245–4287.
- 1072 Lin, S.-J. (2004). A 'vertically Lagrangian' finite-volume dynamical core for global
1073 models. *Mon. Wea. Rev.*, 132, 2293-2307.
- 1074 Lin, S.-J., & Rood, R. B. (1997). An explicit flux-form semi-Lagrangian shallow-
1075 water model on the sphere. *Q.J.R.Meteorol.Soc.*, 123, 2477-2498.
- 1076 Lipscomb, W. H., Fyke, J. G., Vizcaíno, M., Sacks, W. J., Wolfe, J., Vertenstein,
1077 M., ... Lawrence, D. M. (2013). Implementation and initial evaluation of the
1078 glimmer community ice sheet model in the community earth system model.
1079 *Journal of Climate*, 26(19), 7352–7371.
- 1080 Loeb, N. G., Doelling, D. R., Wang, H., Su, W., Nguyen, C., Corbett, J. G., ...
1081 Kato, S. (2018). Clouds and the earth's radiant energy system (ceres) energy
1082 balanced and filled (ebaf) top-of-atmosphere (toa) edition-4.0 data product.
1083 *Journal of Climate*, 31(2), 895–918.
- 1084 Lofverstrom, M., Fyke, J. G., Thayer-Calder, K., Muntjewerf, L., Vizcaino, M.,
1085 Sacks, W. J., ... Bradley, S. L. (2020). An efficient ice sheet/earth sys-
1086 tem model spin-up procedure for cesm2-cism2: Description, evaluation, and
1087 broader applicability. *Journal of Advances in Modeling Earth Systems*, 12(8),
1088 e2019MS001984.
- 1089 Morlighem, M., Rignot, E., Mouginot, J., Seroussi, H., & Larour, E. (2014). Deeply
1090 incised submarine glacial valleys beneath the greenland ice sheet. *Nature Geo-*
1091 *science*, 7(6), 418–422.
- 1092 Mottram, R., Boberg, F., Langen, P., Yang, S., Rodehacke, C., Christensen, J. H.,
1093 & Madsen, M. S. (2017). Surface mass balance of the greenland ice sheet in
1094 the regional climate model hirham5: Present state and future prospects. *Low*
1095 *Temp. Sci.*, 75, 105–115.
- 1096 Muntjewerf, L., Sacks, W. J., Lofverstrom, M., Fyke, J., Lipscomb, W. H., Er-
1097 nani da Silva, C., ... Sellevold, R. (2021). Description and Demonstration of
1098 the Coupled Community Earth System Model v2–Community Ice Sheet Model
1099 v2 (CESM2-CISM2). *Journal of Advances in Modeling Earth Systems*, 13(6),
1100 e2020MS002356.
- 1101 Neale, R. B., Richter, J. H., & Jochum, M. (2008). The impact of convection on
1102 ENSO: From a delayed oscillator to a series of events. *J. Climate*, 21, 5904-
1103 5924.
- 1104 Noël, B., Van De Berg, W., Van Meijgaard, E., Kuipers Munneke, P., Van De Wal,
1105 R., & Van Den Broeke, M. (2015). Evaluation of the updated regional climate

- model racmo2. 3: summer snowfall impact on the greenland ice sheet. *The Cryosphere*, 9(5), 1831–1844.
- Noël, B., van de Berg, W. J., Lhermitte, S., & van den Broeke, M. R. (2019). Rapid ablation zone expansion amplifies north greenland mass loss. *Science advances*, 5(9), eaaw0123.
- Noël, B., van de Berg, W. J., Van Wessem, J. M., Van Meijgaard, E., Van As, D., Lenaerts, J., ... others (2018). Modelling the climate and surface mass balance of polar ice sheets using racmo2-part 1: Greenland (1958–2016). *The Cryosphere*, 12(3), 811–831.
- Obrien, T. A., Collins, W. D., Kashinath, K., Rübel, O., Byna, S., Gu, J., ... Ullrich, P. A. (2016). Resolution dependence of precipitation statistical fidelity in hindcast simulations. *J. Adv. Model. Earth Syst.*, 8(2), 976–990. Retrieved from <http://dx.doi.org/10.1002/2016ms000671> doi: 10.1002/2016ms000671
- Ohmura, A. (2001). Physical basis for the temperature-based melt-index method. *Journal of applied Meteorology*, 40(4), 753–761.
- Pfister, G. G., Eastham, S. D., Arellano, A. F., Aumont, B., Barsanti, K. C., Barth, M. C., ... others (2020). The multi-scale infrastructure for chemistry and aerosols (musica). *Bulletin of the American Meteorological Society*, 101(10), E1743–E1760.
- Pollard, D. (2010). A retrospective look at coupled ice sheet–climate modeling. *Climatic Change*, 100(1), 173–194.
- Pollard, D., & Groups, P. P. (2000). Comparisons of ice-sheet surface mass budgets from paleoclimate modeling intercomparison project (pmip) simulations. *Global and Planetary Change*, 24(2), 79–106.
- Pope, V., & Stratton, R. (2002). The processes governing horizontal resolution sensitivity in a climate model. *Climate Dynamics*, 19(3-4), 211–236.
- Putman, W. M., & Lin, S.-J. (2007). Finite-volume transport on various cubed-sphere grids. *J. Comput. Phys.*, 227(1), 55–78.
- Rae, J., Adalgeirsdóttir, G., Edwards, T. L., Fettweis, X., Gregory, J., Hewitt, H., ... others (2012). Greenland ice sheet surface mass balance: evaluating simulations and making projections with regional climate models. *The Cryosphere*, 6(6), 1275–1294.
- Rasch, P. J., & Williamson, D. L. (1990). Computational aspects of moisture transport in global models of the atmosphere. *Q. J. R. Meteorol. Soc.*, 116, 1071–1090.
- Reeh, N. (1991). Parameterization of melt rate and surface temperature in the greenland ice sheet. *Polarforschung*, 59(3), 113–128.
- Rhoades, A. M., Huang, X., Ullrich, P. A., & Zarzycki, C. M. (2016). Characterizing sierra nevada snowpack using variable-resolution cesm. *Journal of Applied Meteorology and Climatology*, 55(1), 173–196. Retrieved from <https://doi.org/10.1175/JAMC-D-15-0156.1> doi: 10.1175/JAMC-D-15-0156.1
- Richter, J. H., Sassi, F., & Garcia, R. R. (2010). Toward a physically based gravity wave source parameterization in a general circulation model. *J. Atmos. Sci.*, 67, 136–156. doi: dx.doi.org/10.1175/2009JAS3112.1
- Rignot, E., & Mouginot, J. (2012). Ice flow in greenland for the international polar year 2008–2009. *Geophysical Research Letters*, 39(11).
- Roeckner, E., Brokopf, R., Esch, M., Giorgetta, M., Hagemann, S., Kornblueh, L., ... Schulzweida, U. (2006). Sensitivity of simulated climate to horizontal and vertical resolution in the echam5 atmosphere model. *Journal of Climate*, 19(16), 3771–3791.
- Sellevold, R., Van Kampenhout, L., Lenaerts, J., Noël, B., Lipscomb, W. H., & Vizcaino, M. (2019). Surface mass balance downscaling through elevation classes in an earth system model: Application to the greenland ice sheet. *The Cryosphere*, 13(12), 3193–3208.

- 1161 Serreze, M. C., Barrett, A. P., Slater, A. G., Steele, M., Zhang, J., & Trenberth,
 1162 K. E. (2007). The large-scale energy budget of the arctic. *Journal of Geophysical*
 1163 *Research: Atmospheres*, 112(D11).
- 1164 Simmons, A. J., & Jiabin, C. (1991). The calculation of geopotential and
 1165 the pressure gradient in the ECMWF atmospheric model: Influence on
 1166 the simulation of the polar atmosphere and on temperature analyses.
Quart. J. Roy. Meteor. Soc., 117(497), 29-58. Retrieved from <https://rmet.s.onlinelibrary.wiley.com/doi/abs/10.1002/qj.49711749703> doi:
 1167 <https://doi.org/10.1002/qj.49711749703>
- 1170 Small, R. J., Bacmeister, J., Bailey, D., Baker, A., Bishop, S., Bryan, F., ... Verten-
 1171 stein, M. (2014). A new synoptic scale resolving global climate simulation
 1172 using the community earth system model. *J. Adv. Model. Earth Syst.*, 6(4),
 1173 1065–1094. doi: 10.1002/2014MS000363
- 1174 Suarez, M. J., & Takacs, L. L. (1995). Volume 5 documentation of the aries/geos dy-
 1175 namical core: Version 2.
- 1176 Taylor, M. A., & Fournier, A. (2010). A compatible and conservative spectral el-
 1177 ement method on unstructured grids. *J. Comput. Phys.*, 229(17), 5879 - 5895.
 1178 doi: 10.1016/j.jcp.2010.04.008
- 1179 Taylor, M. A., Guba, O., Steyer, A., Ullrich, P. A., Hall, D. M., & Eldred, C.
 1180 (2020). An energy consistent discretization of the nonhydrostatic equations
 1181 in primitive variables. *Journal of Advances in Modeling Earth Systems*, 12(1).
 1182 doi: 10.1029/2019MS001783
- 1183 Taylor, M. A., Tribbia, J., & Iskandarani, M. (1997). The spectral element method
 1184 for the shallow water equations on the sphere. *J. Comput. Phys.*, 130, 92-108.
- 1185 Team, E. J. S., Balaji, V., Boville, B., Collins, N., Craig, T., Cruz, C., ... others
 1186 (2021). *Esmf user guide* (Tech. Rep.).
- 1187 Tedesco, M., & Alexander, P. (2013). Modis (mod10a1) albedo data on the mar rcm
 1188 grid (2000–2013). URL: <https://cds.climate.copernicus.eu>. doi: 10.18739/
 1189 A2SK7T
- 1190 Ullrich, P. A., & Taylor, M. A. (2015). Arbitrary-order conservative and consis-
 1191 tent remapping and a theory of linear maps: Part i. *Monthly Weather Review*,
 1192 143(6), 2419–2440.
- 1193 Ullrich, P. A., Zarzycki, C. M., McClenny, E. E., Pinheiro, M. C., Stansfield, A. M.,
 1194 & Reed, K. A. (2021). Tempestextremes v2. 1: a community framework for
 1195 feature detection, tracking and analysis in large datasets. *Geoscientific Model*
 1196 *Development Discussions*, 1–37.
- 1197 Van Angelen, J., Lenaerts, J., Lhermitte, S., Fettweis, X., Kuipers Munneke, P.,
 1198 Van den Broeke, M., ... Smeets, C. (2012). Sensitivity of greenland ice
 1199 sheet surface mass balance to surface albedo parameterization: a study with a
 1200 regional climate model. *The Cryosphere*, 6(5), 1175–1186.
- 1201 van Kampenhout, L., Lenaerts, J. T., Lipscomb, W. H., Lhermitte, S., Noël, B.,
 1202 Vizcaíno, M., ... van den Broeke, M. R. (2020). Present-day greenland ice
 1203 sheet climate and surface mass balance in cesm2. *Journal of Geophysical*
 1204 *Research: Earth Surface*, 125(2).
- 1205 Van Kampenhout, L., Rhoades, A. M., Herrington, A. R., Zarzycki, C. M., Lenaerts,
 1206 J., Sacks, W. J., & Van Den Broeke, M. R. (2019). Regional grid refinement
 1207 in an earth system model: impacts on the simulated greenland surface mass
 1208 balance. *The Cryosphere*, 13(6), 1547–1564.
- 1209 Wan, H., Giorgetta, M. A., Zängl, G., Restelli, M., Majewski, D., Bonaventura, L.,
 1210 ... others (2013). "the icon-1.2 hydrostatic atmospheric dynamical core on
 1211 triangular grids, part i: formulation and performance of the baseline version".
Geosci. Model Dev., 6, 735–763.
- 1212 Williamson, D. (2007). The evolution of dynamical cores for global atmospheric
 1213 models. *J. Meteor. Soc. Japan*, 85, 241-269.
- 1214 Williamson, D. (2008). Convergence of aqua-planet simulations with increasing res-

- 1216 olution in the community atmospheric model, version 3. *Tellus A*, 60(5), 848–
1217 862. doi: 10.1111/j.1600-0870.2008.00339.x
- 1218 Zarzycki, C. M., Jablonowski, C., & Taylor, M. A. (2014). Using variable-resolution
1219 meshes to model tropical cyclones in the community atmosphere model. *Mon.*
1220 *Wea. Rev.*, 142(3), 1221–1239. doi: 10.1175/MWR-D-13-00179.1
- 1221 Zhang, G., & McFarlane, N. (1995). Sensitivity of climate simulations to the
1222 parameterization of cumulus convection in the canadian climate center general-
1223 circulation model. *ATMOSPHERE-OCEAN*, 33(3), 407–446.

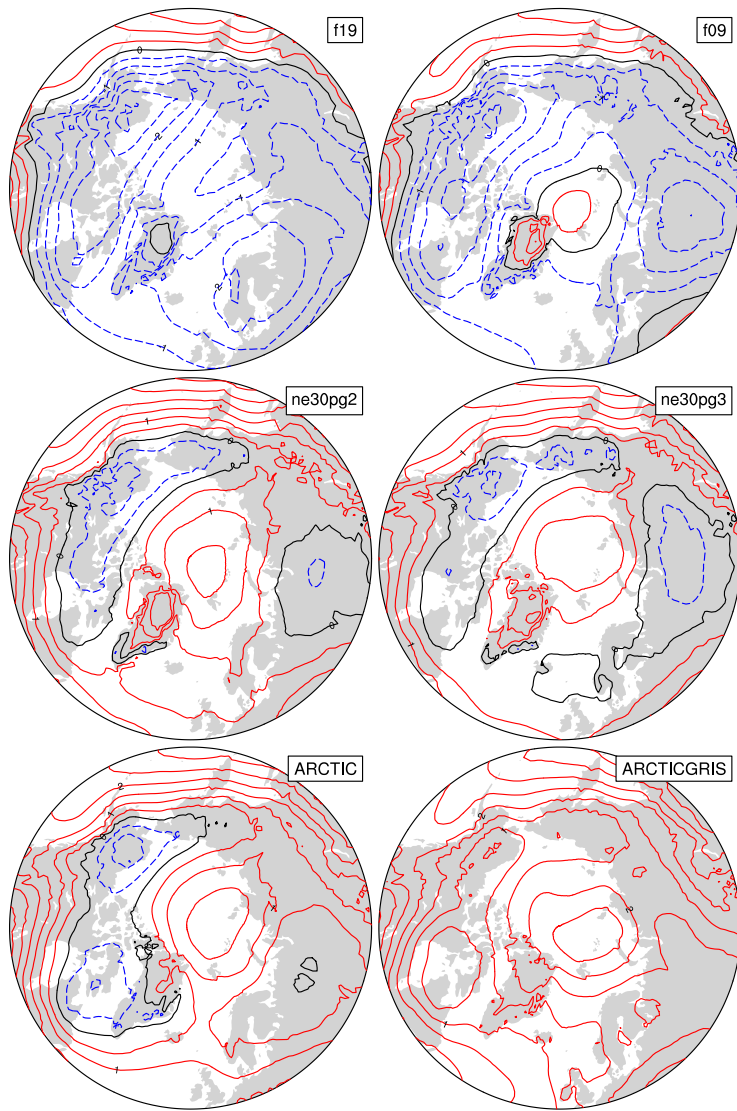


Figure 6. 1979-1998 lower troposphere, northern hemisphere summer virtual temperature biases, computed as the difference from ERA5. Lower troposphere layer mean virtual temperature is derived from the 1000 hPa - 500h Pa geopotential thickness, using the hypsometric equation. Differences are computed after mapping the ERA5 data to the finite-volume grids since the geopotential field is only available on the output tapes in the spectral-element runs that have been interpolated to the f09 grid, inline.

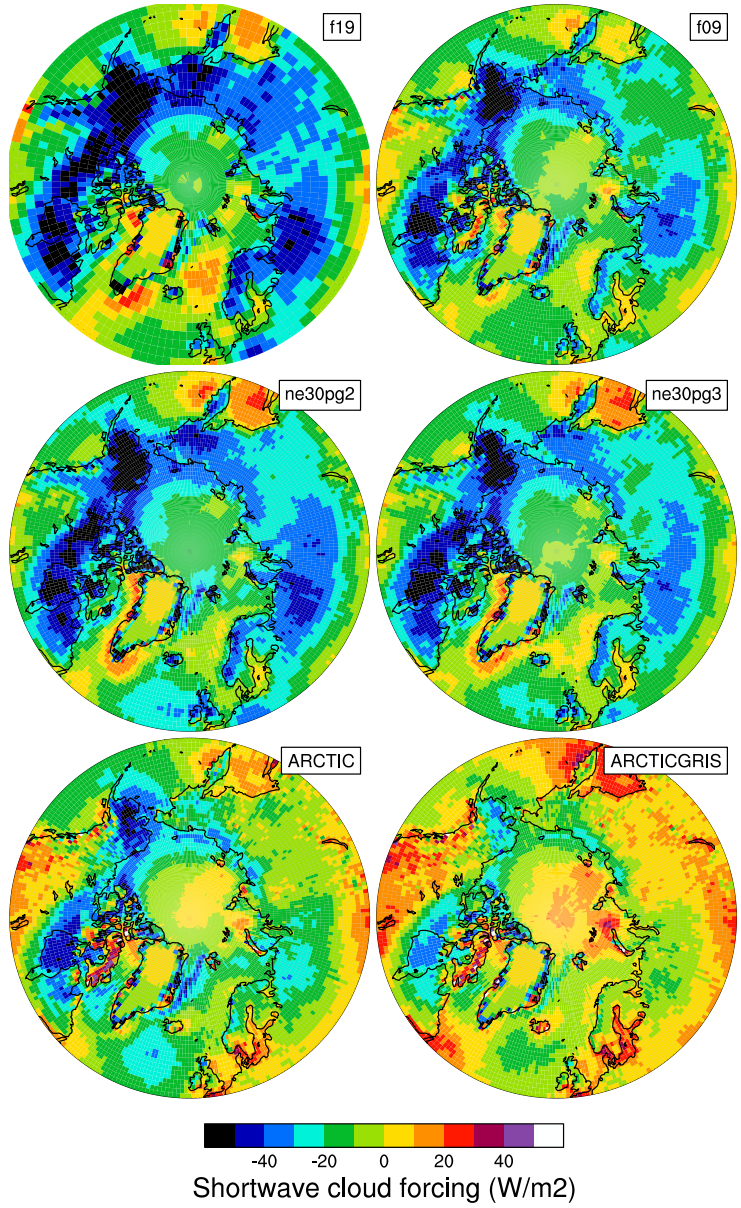


Figure 7. 1979-1998 Northern Hemisphere summer shortwave cloud forcing bias, relative to the CERES-EBAF gridded dataset. Shortwave cloud forcing is defined as the difference between all-sky and clear-sky net shortwave fluxes at the top of the atmosphere. Differences are computed after mapping all model output to the 1° CERES-EBAF grid.

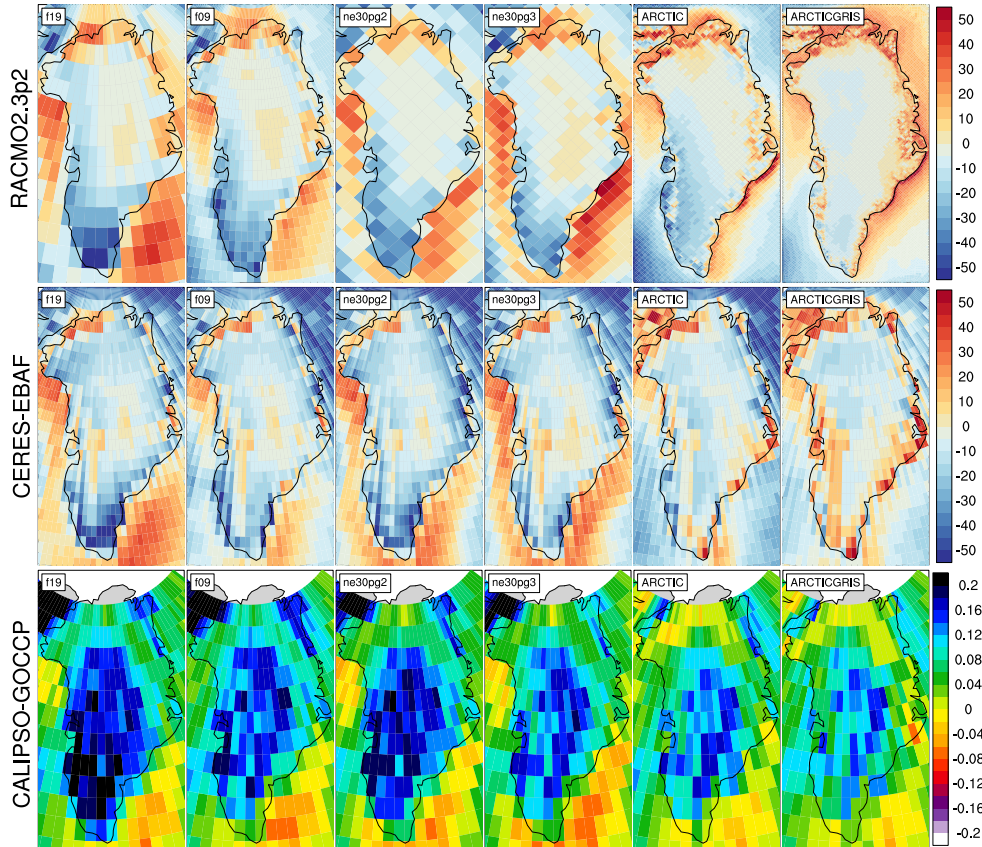


Figure 8. 1979-1998 northern hemisphere summer surface incident shortwave radiation bias (W/m^2), computed as the difference (top) from RACMO2.3p2, and (middle) the CERES-EBAF dataset, and the (bottom) total cloud fraction bias relative to the CALIPSO dataset. CALIPSO and CERES differences are found by mapping the model output to the 1° grid, and differences in the bottom panel are computed after mapping the RACMO2.3p2 dataset to the individual model grids. Note that the averaging period for the CALIPSO-GOCCP and CERES-EBAF panels, 2006-2017 and 2003-2020, respectively, are different from the averaging period for the model results.

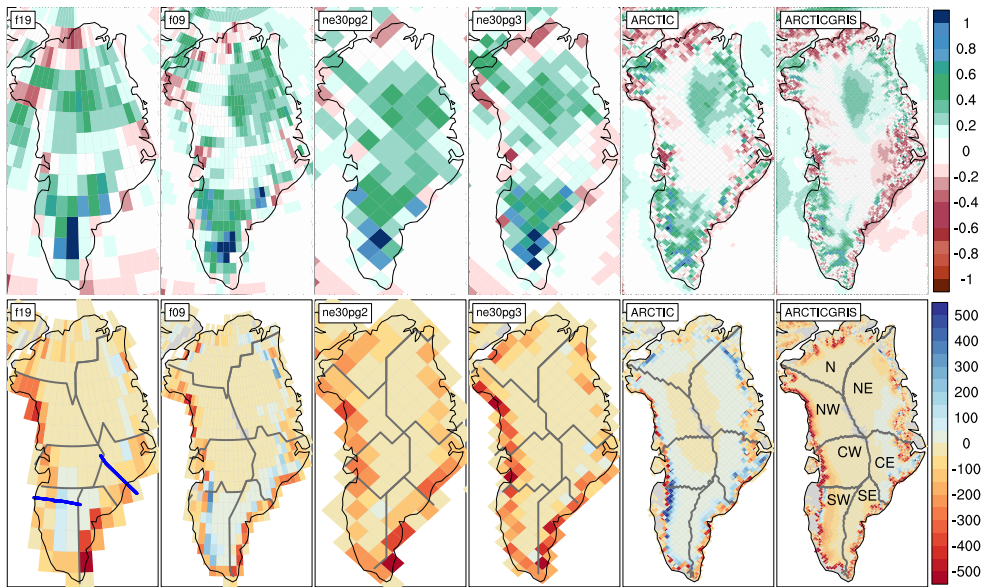


Figure 9. 1979-1998 (top) annual precipitation and (bottom) ice/snow melt biases relative to RACMO2.3p2, evaluated on the native model grids. The precipitation biases are expressed as fractional changes, whereas the melt biases are absolute changes (mm/yr). In the bottom panel, the Rignot and Mouginot (2012) basin boundaries are shown in grey for each model grid. Note that Figure 11 uses the basin boundaries for the two common ice masks, shown in the **f19** and **ne30pg2** panels, in computing the basin-scale integrals. Blue lines in the **f19** panel show the location of the two transects plotted in Figure 12.

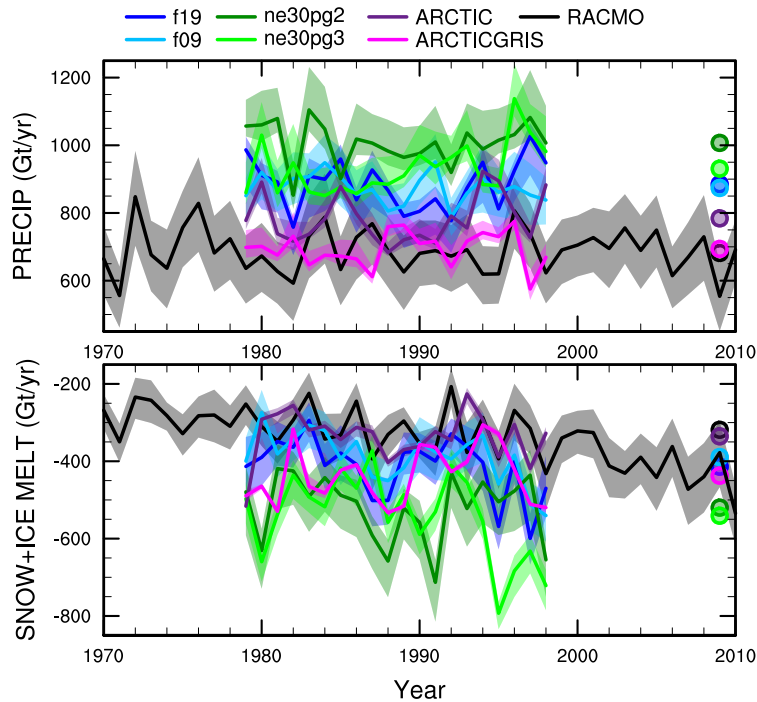


Figure 10. Time-series of annual (solid+liquid) precipitation (top) and annual runoff (bottom) integrated over the Greenland Ice Sheet for all six simulations and compared to the RACMO datasets. The time-series were generated using the common ice mask approach, which results in up to 4 ensembles, with the mean value given by the solid line and shading spanning the extent of the ensemble members.

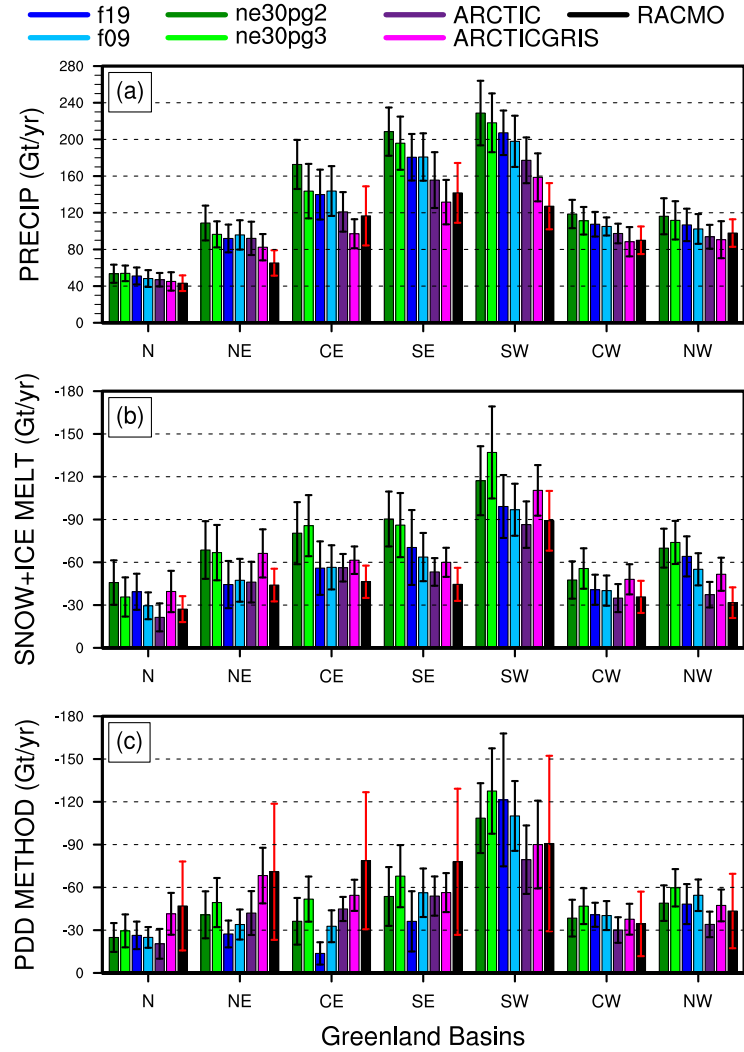


Figure 11. 1979–1998 basin integrated components of the SMB; (top) precipitation, (middle) ice/snow melt and (bottom) ice/snow melt estimated from the PDD method. Whiskers span the max/min of the four ensemble members generated from the common-ice-mask approach. Basin definitions are after Rignot and Mouginot (2012), and are found on the common ice masks using a nearest neighbor approach, and shown in Figure 9.

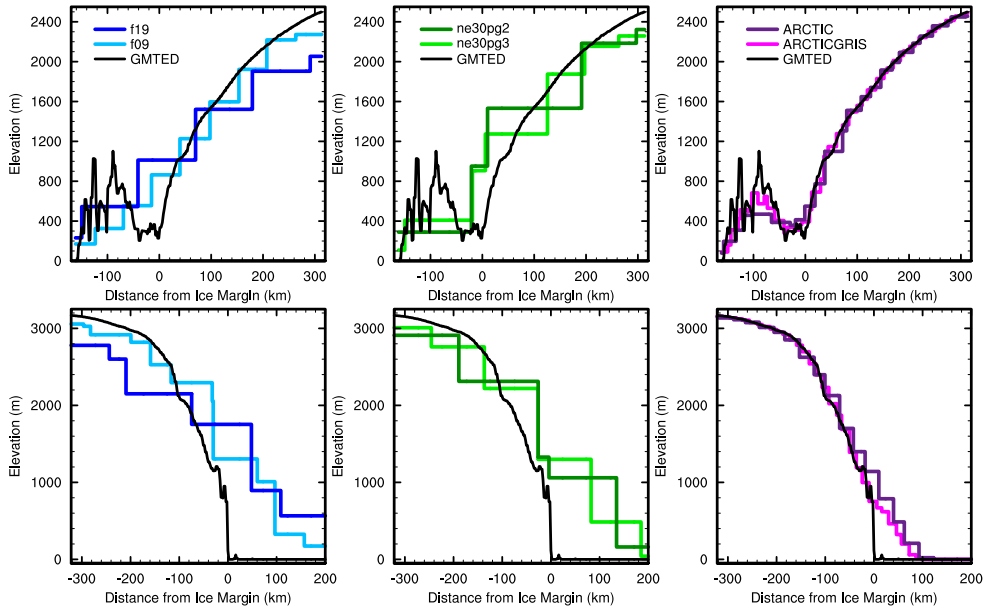


Figure 12. Model surface elevation along the (top) K-transect, and (bottom) a transect spanning the central dome down to the Kangerlussuaq glacier in southeast Greenland, for all model grids. The GMTED reference surface is a 1 km surface elevation dataset (J. Danielson & Gesch, 2011) used for generating the CAM topographic boundary conditions.

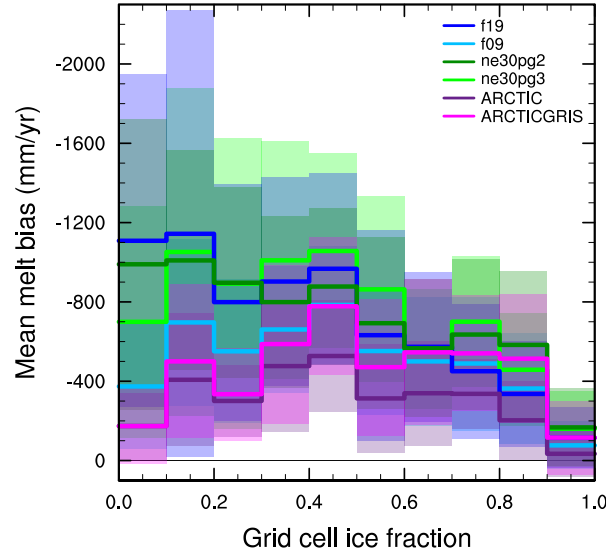


Figure 13. Fractional melt bias over the GrIS, computed relative to the RACMO datasets using the common ice mask approach, and conditionally sampled by grid cell ice fraction provided by the common ice masks. Solid lines are the mean of the distribution with \pm one standard deviation expressed by shading.

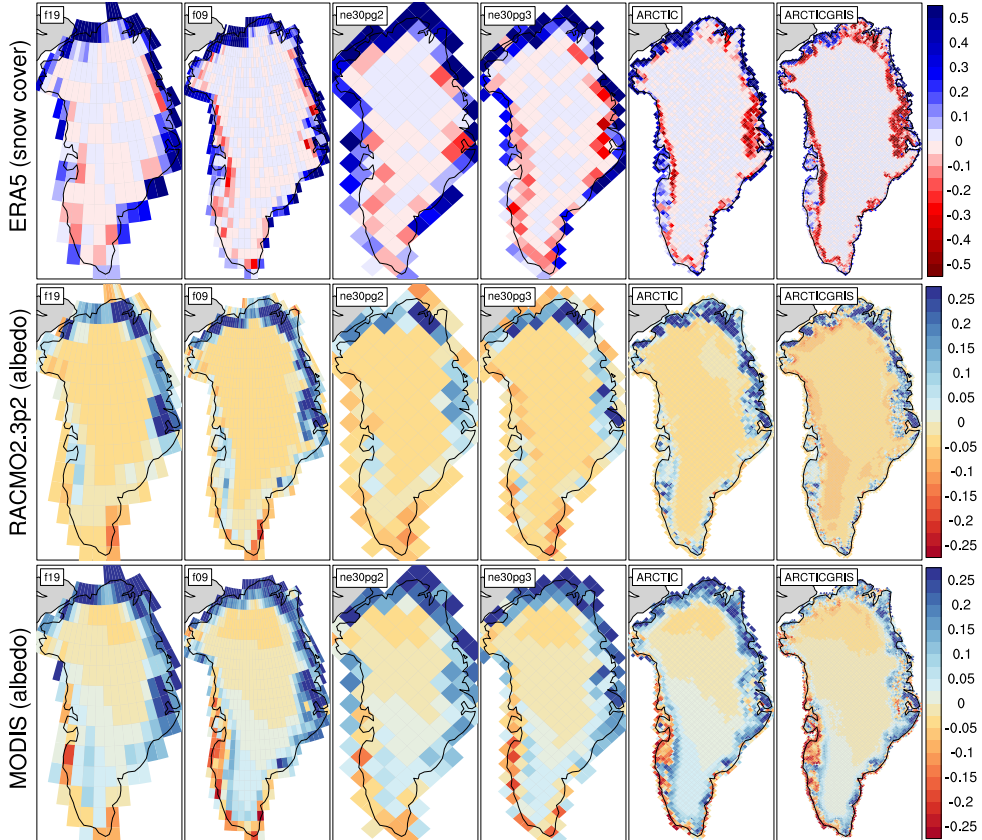


Figure 14. (Top) 1979-1998 bias in northern hemisphere summer snow cover (fraction) relative to ERA4. (Middle and bottom) 1979-1998 summer albedo bias (fraction), computed as the difference (middle) from RACMO2.3p2, and (bottom) the MODIS dataset of Tedesco and Alexander (2013). As all observational datasets in this plot are on high-resolution grids, they've all been mapped to the individual model grids, before taking differences.

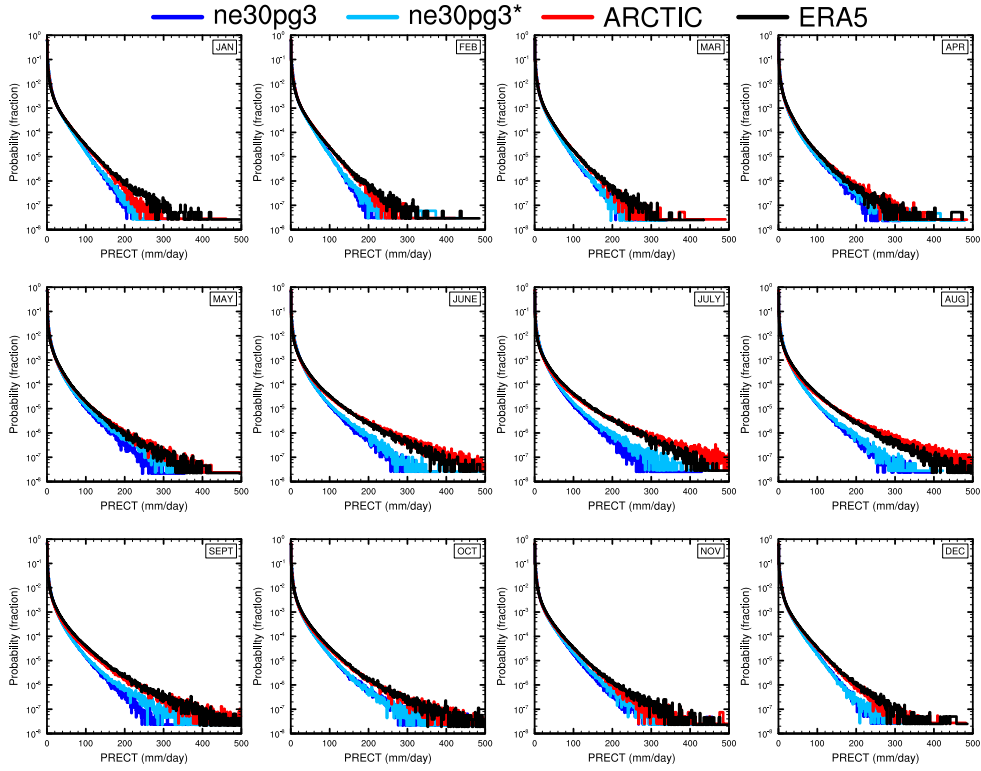


Figure 15. PDFs of the total precipitation rate associated with tracked storms, by month, in the ne30pg3, ne30pg3* and Arctic runs, and compared with the ERA5 dataset.

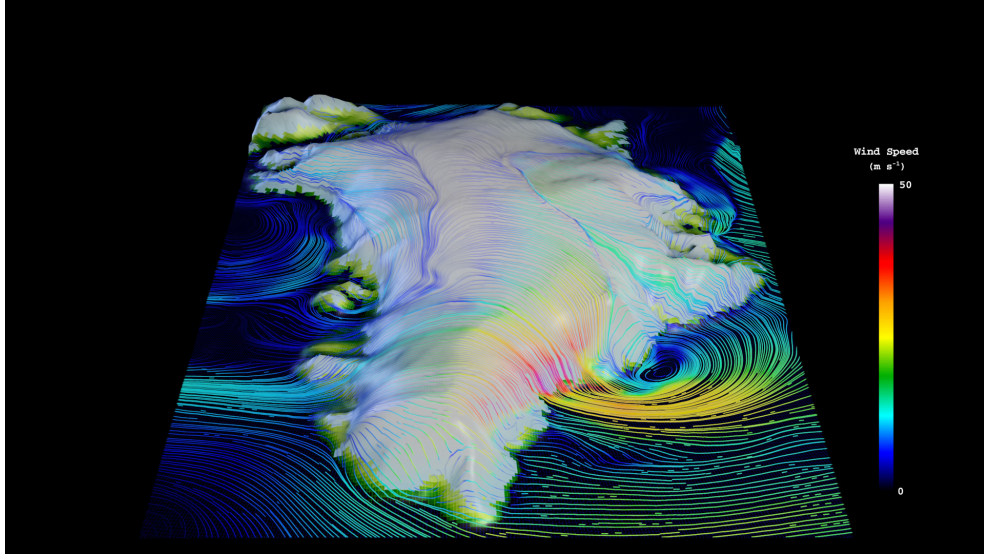


Figure 16. Snapshot of the lowest model level streamlines from the Arctic – GrIS visualization, with color shading denoting the wind magnitude.

OMEGA500, 1 year average, F2000climo, 32 levels

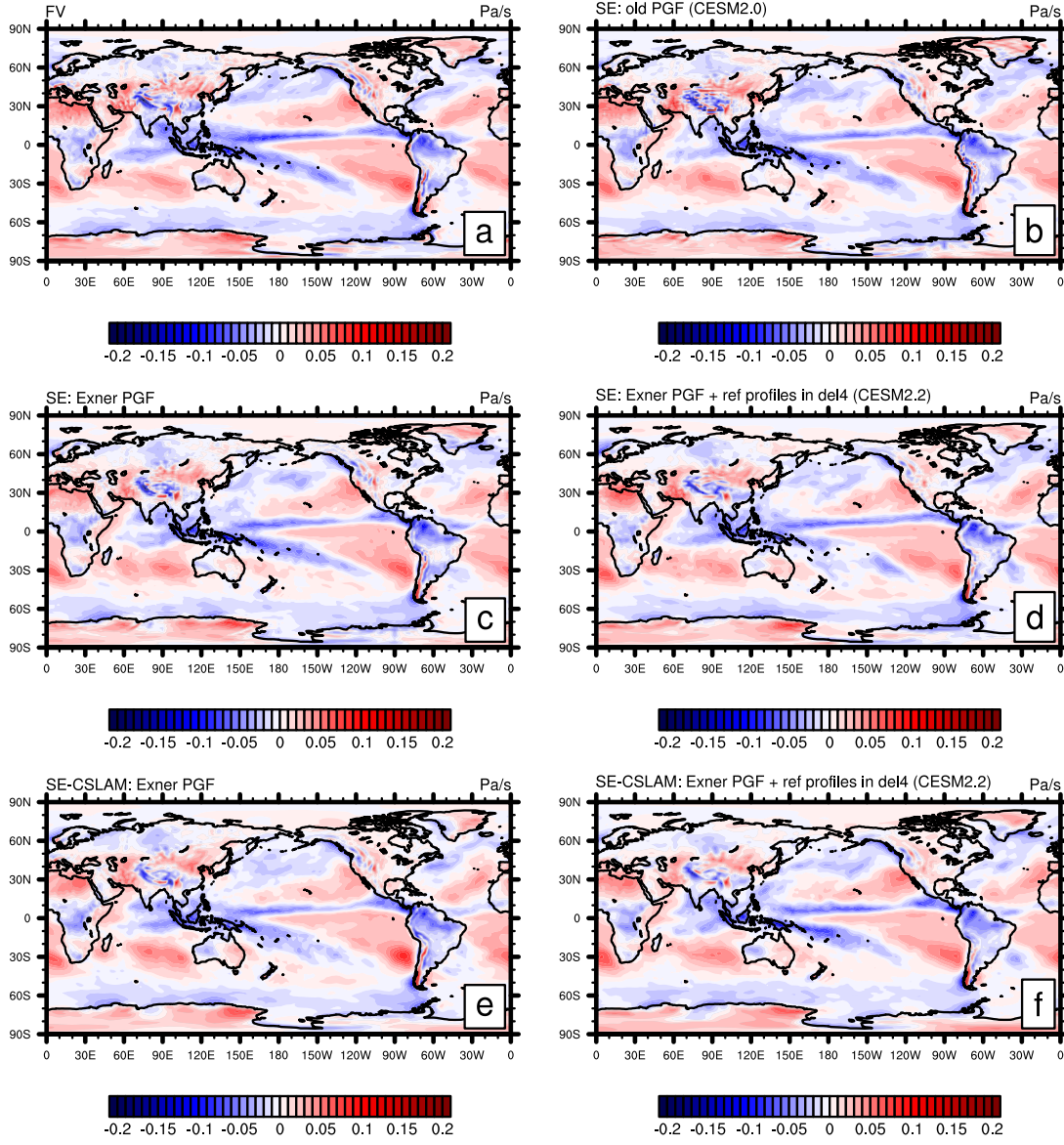


Figure A1. One year averages of vertical pressure velocity at 500hPa (OMEGA500) using (a) CAM-FV (Finite-Volume dynamical core) and (b-f) various versions of the spectral-element (SE) dynamical core at approximately 1° horizontal resolution and using 32 levels. (b) is equivalent to the CESM2.0 version of the SE dynamical core using the "traditional"/"old" discretization of the pressure-gradient force (PGF). Plot (c) is equivalent to configuration (b) but using the Exner form of the PGF. Plot (d) is the same as configuration (c) but also subtracting reference profiles from pressure and temperature before applying hyperviscosity operators (which is equivalent to the CESM2.2 version of SE in terms of the dynamical core). Plots (e) and (f) are equivalent to (c) and (d), respectively, by using the SE-CSLAM (ne30pg3) version of the SE dynamical core (i.e. separate quasi-uniform physics grid and CSLAM transport scheme).

OMEGA500, 18 months average, FHS94 forcing, 32 levels

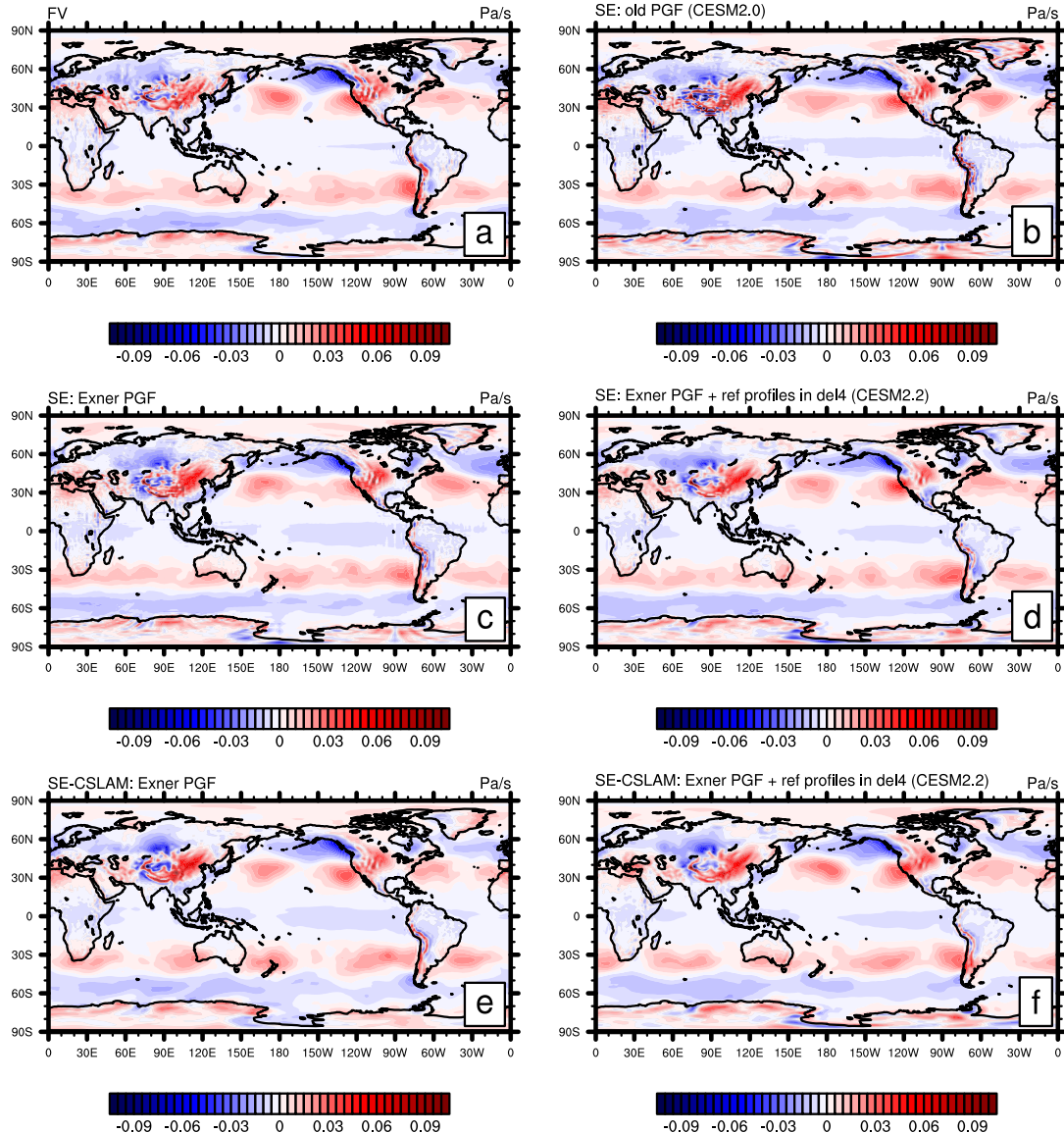


Figure A2. Same as Figure A1 but using modified Held-Suarez forcing and the average is over 18 months (excl. spin-up).